Contributions to Mineralogy and Petrology (2025) 180:84
https://doi.org/10.1007/s00410-025-02272-y

ORIGINAL PAPER

The solubility of molecular hydrogen in silicate melts and the origin of hydrogen in the interiors of terrestrial planets

Alok Chaudhari[1,2] · Matteo Masotta[1,3] · Svyatoslav Shcheka[1,4] · Hans Keppler[1]

Received: 29 April 2025 / Accepted: 14 September 2025 / Published online: 8 October 2025
© The Author(s) 2025

Abstract

The solubility of molecular hydrogen (H_2) was measured in haplogranite, andesite, and basalt (MORB) melt. Experiments were carried out with rapid-quench TZM vessels and a piston cylinder apparatus at 0.2 GPa −4 GPa, 1100 ˚C −1400 ˚C, and iron-wüstite (Fe-FeO) buffer conditions. H_2 contents in quenched glasses were measured by infrared (FTIR) spectroscopy. For this purpose, the infrared extinction coefficient of the 4120 cm^{-1} band of H_2 in haplogranitic glass was re-calibrated by two independent methods. This yielded a linear molar extinction coefficient of (2.12 ± 0.05) liter $mol^{-1}cm^{-1}$, which is about one order of magnitude larger than a coefficient used in previous studies. The new extinction coefficient was used to quantify H_2 solubility in all glass samples of this study. The solubility of molecular hydrogen increases with increasing pressure, being higher in haplogranite than in andesitic or basaltic melt, as expected from ionic porosity considerations. The data at Fe-FeO buffer conditions can all be reproduced by a simple Henry style solubility law $c_{H2} = a_{Henry} P$, with a_{Henry} = (206 ± 10) ppm/GPa for basalt, (362 ± 35) ppm/GPa for andesite, and (500 ± 62) ppm/GPa for haplogranite, where ppm is ppm H_2 by weight (μg/g). However, due to the use of an erroneous infrared extinction coefficient, previous studies may have overestimated H_2 solubility in silicate melts by about one order of magnitude. According to the new data presented here, H_2 dissolution in a magma ocean is not a very efficient mechanism for generating elevated hydrogen contents in planetary interiors. Equilibrium thermodynamic modelling shows that in an Earth with chondritic bulk composition, even at an oxygen fugacity six log units below the Fe-FeO buffer, the molar ratio of H_2/H_2O in the magma ocean is still below unity. At a more plausible oxygen fugacity two log units below Fe-FeO, the ratio is 0.06. However, the strong partitioning of hydrogen into the atmosphere under the very reducing conditions of early accretion may have enhanced hydrogen loss due to hydrodynamic escape and impact erosion. Possibly, this was a decisive mechanism for depleting the Earth in volatiles as compared to its chondritic building blocks.

Keywords Hydrogen · Water · Magma ocean · Primordial atmosphere · Infrared · Extinction coefficient · Planetary evolution · Volatiles · Chondrites · Accretion

Introduction

In volcanic gases on modern Earth, H_2 is only a minor or trace component (e.g., Symonds et al. 1994). Under the reducing conditions prevailing deeper in Earth´s mantle, H_2 may become a major species in aqueous fluids and perhaps even a significant species of dissolved hydrogen in nominally anhydrous minerals (Yang et al. 2016; Moine et al. 2020). Moreover, molecular hydrogen was the main component of the solar nebula during the formation of the solar system and the magma ocean on Earth and Moon may have equilibrated with a hydrogen-rich atmosphere (e.g. Elkins-Tanton and Grove 2011; Gaillard et al. 2022). For this reason, the solubility of H_2 in silicate melts has received

Communicated by Dante Canil

✉ Hans Keppler
hans.keppler@uni-bayreuth.de

[1] Bayerisches Geoinstitut, Universität Bayreuth, 95440 Bayreuth, Germany

[2] Present address: CSIRO, Kensington, Perth, WA 6151, Australia

[3] Present address: Dipartimento di Scienze della Terra, Università di Pisa, Pisa, Italy

[4] Present address: School of Earth and Oceans, University of Western Australia, Perth, WA 6009, Australia

considerable attention in recent years, as the dissolution of H_2 in the magma ocean may have contributed to or even dominated the initial hydrogen reservoir in the mantle (Hirschmann et al. 2012; Gaillard et al. 2022; Young et al. 2023). Hydrogen partitioning between metal and the magma ocean may even have established a major hydrogen reservoir in Earth´s core (Young et al. 2023).

Luth et al. (1987) detected the Raman band of dissolved H_2 at 4125 cm^{-1} in glasses quenched from sodium silicate and sodium alumosilicate melts equilibrated at Fe-FeO buffer conditions. However, in the absence of a suitable calibration of Raman intensities, they could not quantify the concentration of H_2 dissolved in the melts. Early phase equilibrium studies (Schmidt et al. 1997; see also Schmidt et al. 1999) essentially considered H_2 to be an inert component with very low solubility in silicate melts. This was consistent with the observation that the effect of H_2 on the solidus in the haplogranite-H_2O-H_2 system is very similar to the effects of N_2 or CO_2 in the haplogranite-H_2O-N_2 and haplogranite-H_2O-CO_2 systems. Hirschmann et al. (2012) suggested that dissolved H_2 may actually have been a significant species of hydrogen in the early magma ocean and also in melts in the deep mantle of the modern Earth. The latter study, however, was mainly based on the quantification of dissolved H_2 concentrations in quenched glasses using infrared spectroscopy and the infrared extinction coefficient (e.g., Ihinger et al. 1994) for H_2 reported by Shelby et al. (1994). This method of quantifying dissolved H_2, however, is rather questionable for two reasons: (i) The extinction coefficient of Shelby et al. (1994) was calibrated for pure silica glass and may not be applicable to glasses with the composition of natural magmas, as infrared extinction coefficients are generally matrix-dependent. For H_2, this matrix-dependence may be particularly strong, as the H_2 molecule has no permanent dipole moment and the infrared activity is only activated by interactions with the glass matrix, which induces a minor dipole moment. (ii) The coefficient of Shelby et al. (1994) was determined by a simple gravimetric method, which attributed the weight loss of H_2-loaded silica glass upon heating exclusively to the loss of H_2. This is obviously a rather questionable assumption. Some of the weight loss may have been caused by the desorption of material on the surface or of other trace volatile components that were trapped inside the glass itself. If such effects occurred, they would imply that the extinction coefficient of Shelby et al. (1994) may be too low, with the consequence that any study that relies on this coefficient may greatly overestimate H_2 solubility in silicate melts. Gaillard et al. (2003) indirectly inferred hydrogen solubility in silicic melts by kinetic modelling of the redox exchange between hydrogen and iron in the melt, with results that are roughly consistent with those of Hirschmann et al. (2012). Very recently, Foustoukos (2025) studied the partitioning of H_2 between aqueous fluids and hydrous silicate melts by in-situ Raman spectroscopy in diamond cells. However, the quantification of H_2 concentrations in the melt was based on the unlikely assumption that the scattering coefficients of H_2 in the melt and in the fluid and all other parameters influencing scattering efficiency in the two phases are equal.

In the current study, we re-visited H_2 solubility in silicate melt. In order to constrain the effect of melt composition on H_2 solubility, we studied haplogranitic, andesitic, and basaltic melts up to 4 GPa and 1400 ˚C. For accurate quantification of H_2, we re-calibrated the infrared extinction coefficient of H_2 in silicate glasses using the haplogranitic system as a model. Rather than relying on a weight loss method, we calibrated the infrared extinction coefficient for H_2-loaded haplogranitic glasses using two independent methods: (i) We used Karl Fischer titration to determine the total H content in the glasses and subtracted the H_2O content obtained by infrared spectroscopy to obtain the concentration of hydrogen present as H_2. (ii) We treated the H_2-bearing glasses at high pressure in a pure O_2 atmosphere, such that any H_2 present was oxidized to H_2O. The corresponding increase in H_2O concentration was again determined by infrared spectroscopy.

Methods

Starting materials

The starting materials were three synthetic glasses with compositions equivalent to a Fe-free Mid Ocean Ridge Basalt (MORB), a Fe-free andesite and a haplogranite. Compared to natural compositions, FeO was replaced by the equimolar amount of MgO + CaO, with a molar Mg : Ca ratio of 1. Fe-free compositions were chosen to avoid any complications due to possible redox reactions of H_2 with ferric iron. Glasses were synthesized from stoichiometric mixtures of analytical-grade SiO_2, Na_2CO_3, K_2CO_3, $Al(OH)_3$, $Mg(OH)_2$, TiO_2, and $CaCO_3$. The mixtures were decarbonated and dehydrated in a platinum crucible by slowly heating in a furnace from room temperature to 1100 ˚C over 12 h and then maintaining temperature at 1100 ˚C for another 12 h. The crucible with the mixture was then placed at 1600 ˚C in a high temperature box furnace in air for 2 h and afterwards rapidly quenched in distilled water. The resulting glass was finely crushed (< 1 μm) in an agate mortar and the powders were stored in a desiccator. Microprobe analyses of the glasses are given in Table 1.

Table 1 Composition of starting materials

	Basalt (MORB)	Andesite	Haplogranite
SiO_2	51.67 (28)	58.04 (32)	77.24 (74)
TiO_2	1.88 (5)	1.00 (3)	–
Al_2O_3	15.51 (16)	18.19 (11)	11.79 (56)
MgO	10.19 (19)	5.65 (7)	–
CaO	15.84 (15)	11.01 (11)	–
Na_2O	3.53 (9)	3.60 (6)	5.79 (53)
K_2O	0.35 (2)	1.44 (3)	5.36 (17)
Total	99.0	98.9	100.2

Shown are the averages of 40 (basalt and andesite) or 28 (haplogranite) electron microprobe analyses. Numbers in parentheses are one standard deviation in the last digits

Experiments in TZM vessels

Experiments up to 200 MPa and 1100 °C were performed in rapid-quench TZM (Ti and Zr reinforced molybdenum) vessels using argon as pressure medium. The experimental platinum capsules containing the sample were placed on top of a filler rod in the hot zone of the autoclave, held by an external magnet during the experiment. During the quench, the magnet is lowered down and the sample falls into a water-cooled zone. Pressure was determined by employing a mechanical gauge which is accurate up to ± 50 bars. Temperature was measured with an external K type thermocouple in the furnace, calibrated against an internal thermocouple and is accurate up to ± 20 ˚C.

For H_2 solubility measurements in TZM experiments, glass powder was loaded into platinum capsules (5 mm outer diameter, 4.6 mm inner diameter, about 10 mm long) together with about 60 bar of H_2 gas and sealed by arc welding. For gas loading, a device similar to that described by Boettcher et al. (1989) was used. For producing H_2-loaded haplogranitic glasses in TZM vessels for the calibration of the infrared extinction coefficient of H_2, massive cylinders drilled out of haplogranitic glass (3 mm diameter, 10 mm long) were loaded into the platinum capsules (5 mm outer diameter, 4.6 mm inner diameter, 25 mm long), in order to avoid any accidental trapping of H_2 in fluid inclusions. The glass cylinders were embedded into TiO_2 powder as an inert filler material. Hydrogen was introduced in the form of ca. 50 mg of calcium hydride (CaH_2, 90–95%, Thermo Scientific), which was placed below the sample inside a small open crucible made out of fired pyrophyllite that fitted tightly into the capsule. CaH_2 decomposes upon heating to Ca metal and H_2 ($CaH_2 = Ca + H_2$). The pyrophyllite crucible was used to prevent contact of the Ca metal with the Pt capsule. The use of CaH_2 as a hydrogen source has the advantage that larger amounts of H_2 can be introduced into the capsule as compared to direct gas loading of H_2. Moreover, the Ca metal produced by decomposition of CaH_2 upon heating will reduce any traces of H_2O inside the charge to H_2.

One of the methods used to calibrate the infrared extinction coefficient of H_2 is glasses involved the oxidation in a pure O_2 atmosphere. For this, the pieces of H_2-loaded glass retrieved from experiments (also from experiments caried out in the piston cylinder apparatus) were loaded into Pt capsules (3.5 mm outer diameter, 3.2 mm inner diameter, 20 mm length) together with 70 to 80 bars of pure O_2 gas. To oxidize the charge, these capsules were then run at 1100 ˚C and 200 MPa for about 5 h. This was sufficient to oxidize all H_2 to H_2O (see below).

Experiments in the piston cylinder apparatus

H_2 solubility experiments in the pressure range of 0.5 to 4 GPa were carried out with an end-loaded piston cylinder apparatus. The powdered glasses were loaded into platinum capsules and sealed by arc welding. The sealed platinum capsules were placed inside a mechanically sealed iron capsule (outer diameter 5 mm, inner diameter 3.5 mm, length 11 mm), with about 2–3 mg of water. The remaining space between the inner Pt capsule and the iron capsule was filled with analytical grade brucite $Mg(OH)_2$ powder. The usage of iron capsules imposes a hydrogen fugacity equivalent to that of an aqueous fluid in equilibrium with the Fe-FeO oxygen fugacity buffer. Standard 3/4 inch and 1/2 inch assemblies were used for all experiments. The assembly consisted of an outer talc sleeve, a pyrex glass tube and a tapered graphite heater. The iron capsules were surrounded by a boron nitride (BN) sleeve with alumina (Al_2O_3) lids at the end to protect the type S thermocouple. The “hot piston in” technique was used for all of the experiments: The assembly was compressed to 90% of desired pressure and then the remaining 10% pressure was applied after heating the sample to desired temperature. Pressures reported contain a 18% friction correction. The experiments were quenched with a rate of about 100 ˚C/sec by switching off the power.

For producing H_2-saturated haplogranite glass samples for calibrating the infrared extinction coefficient of H_2, again CaH_2 was used as a hydrogen source, as this allows to attain hydrogen fugacities even higher that in equilibrium with Fe and H_2O. Moreover, the Ca metal produced by decomposition of CaH_2 will reduce traces of H_2O to H_2. Again, mechanically sealed Fe capsules were used (outer diameter 5 mm, inner diameter 3 mm, length 10 mm). At the bottom of the capsule, ca. 10–20 mg of CaH_2 were placed, followed by one or two precisely fitting discs of 0.025 mm thick Pt foil. Above this, the haplogranite glass powder (about 40 mg) was filled in, followed by one or two Pt discs and another layer of CaH_2, followed by the mechanically sealing and very tightly fitting iron lid. After the experiments, the Fe

capsules were retrieved intact and cut open with a diamond saw or by grinding away some of the Fe.

Analytical methods

Microprobe analysis. The synthesized starting glasses were mounted in epoxy disks and polished for microprobe analysis. The glasses were analyzed in wavelength - dispersive mode using a JEOL JXA-8900 electron microprobe equipped with 5 detectors. All the glasses were analyzed using accelerating voltage of 15 kV and a sample current of 10 nA. Standards used include albite (Si, Na), orthoclase (K), rutile (Ti), spinel (Al), forsterite (Mg) and andradite (Ca). Around 30–40 spots were selected for each glass (Table 1).

Infrared spectroscopy. Recovered glasses from the solubility experiments were polished on both sides for FTIR analyses. Special precautions were taken during sample polishing, in order to minimize the loss of H_2: The sample thickness was kept as large as possible and samples were prepared without heating the glasses at all. Observations in the course of this study have shown that a significant fraction of H_2 may diffuse out of samples more than 100 µm thick over the course of several months during storage at room temperature. Infrared spectra were measured using a Bruker IFS 120 high-resolution Fourier transform spectrometer coupled with a Bruker IR microscope, equipped with an all-reflecting Cassegrainian optics. The spectrometer is equipped with a permanently aligned Michelson type interferometer. The spectra were collected using a tungsten light source, a Si-coated CaF_2 beam splitter and a narrow-band MCT detector. On average 500–2000 scans were accumulated on each glass at 4 cm^{-1} resolution, using variable aperture sizes on the microscope. Typically, about 5 measurements were carried out at different parts of the sample with spot sizes between 100 and 200 µm. Water contents were quantified based on the absorbance of the 4500 cm^{-1} and 5200 cm^{-1} overtone bands using the extinction coefficients for rhyolitic glasses reported by Withers and Behrens (1999). For converting molar concentrations in wt%, the relationships between density and water content for rhyolitic glasses from Withers and Behrens (1999) were used for the haplogranitic samples and the equations given by Ohlhorst et al. (2001) for the andesitic and basaltic samples.

Raman spectroscopy. Raman spectra were collected for a few glasses using a Horiba Jobin Yvon LabRAM HR800 spectrometer with a Peltier-cooled CCD detector and a 1800 mm^{-1} grating. Samples were measured for 60 s through a 50x microscope objective. The 514 nm line of an argon laser at 200 mW output power was used for excitation.

Karl Fischer-Titration. This method was used to measure the total hydrogen content in some haplogranitic glass samples in order to determine the infrared extinction coefficient of H_2. The instrument used is very similar to the setup described Behrens et al. (1996). It is partially built in-house, with the actual water detection unit being a commercial Mitsubishi (CA-05) moisture analyzer. In principle, the sample is heated in an inductive furnace from room temperature to 1300 ˚C at a rate of 100 ˚C/min. Any gas released is carried by argon through a glass tube containing CuO inside a furnace. The CuO oxidizes any H_2 to H_2O. The argon flow then transports all H_2O into the commercial titration cell, where water is determined through the reaction $I_2 + SO_2 + H_2O = 2\,HI + SO_3$. The I_2 required for this reaction to proceed is generated electrochemically from I^- according to $2\,I^- = I_2 + 2\,e^-$. The electrons released by this reaction are counted and can be converted into moles of water detected. The overall procedure of operation was similar to that described by Behrens et al. (1996), however, with the notable exception that the CuO was kept at a temperature of 600 ˚C to ensure efficient oxidation of H_2 to H_2O. This was tested by using CaH_2 as a sample, which releases only H_2 upon heating. The expected number of moles of H_2 was detected as H_2O in the titration cell. To avoid any H_2 loss or any adsorption of moisture on fine powders, the glass samples were only gently crushed by squeezing them with pliers between aluminum foil immediately before the measurement.

Results

Description of run products

Table 2 summarizes all H_2 solubility experiments that were carried out at Fe-FeO-H_2O buffer conditions in the piston cylinder apparatus. In addition, two exploratory experiments were carried out with haplogranitic glasses and pure H_2 gas in TZM vessels (run AHK01 at 200 MPa, 1100 ˚C for 5 min and AHK04 at 100 MPa, 1100 ˚C and 5 min). The run products from the piston cylinder experiments were glasses without any crystalline phases. Some of the glasses were perfectly clear, some milky, and some run products contained patches of clear and milky glass (Table 2). There is, however, no obvious difference in the infrared spectra of the clear and milky glasses and they generally followed the same solubility trends. Samples produced at 1200˚C and 1300 ˚C in the piston cylinder experiments generally have low water contents (< 1 wt% H_2O). This is expected as the double capsule technique used should allow only H_2 (in form of atomic H) to diffuse into the capsule, not H_2O. However, in the experiments performed at 1400 ˚C, higher water contents up to 3.23 wt% were observed. This suggests

Table 2 Summary of hydrogen solubility experiments at the Fe-FeO-H_2O buffer

No.	Composition	*P* (GPa)	T (˚C)	Duration (min)	Glass	H_2O total (wt%)	H_2 (ppm by weight)
AMPC 5	HPG	1.5	1200	360	milky	0.32	431 (20)
AMPC 6	HPG	1.5	1200	360	milky	1.68	2549 (120)
AMPC 7	HPG	2	1250	270	clear	0.48	594 (27)
AMPC 11	HPG	1	1200	270	milky	0.63	912 (41)
AMPC 14	HPG	2	1300	120	milky	0.95	1137 (52)
AMPC 15	HPG	1.5	1200	15	milky	0.34	1337 (62)
AMPC 16	HPG	1.5	1200	30	milky	0.32	1329 (60)
AMPC 18	HPG	1.5	1200	60	milky	0.36	1108 (50)
AMPC 22	HPG	0.5	1200	180	clear	0.28	320 (15)
AMPC 28	HPG	3	1300	15	part. milky	0.73	1563 (72)
AMPC 29	HPG	4	1300	15	part. milky	0.58	1613 (74)
AMPC 34	HPG	1	1300	15	clear	0.49	816 (37)
AMPC 35	HPG	2	1200	15	milky	0.35	404 (18)
AMPC 37	Andesite	0.5	1400	15	clear	0.60	271 (12)
AMPC 24	Andesite	1	1400	60	milky	0.78	581 (26)
AMPC 23	Andesite	2	1400	120	clear	1.80	793 (36)
AMPC 26	Andesite	2	1400	15	clear	1.8	556 (25)
AMPC 36	Andesite	3	1400	15	clear	2.73	1066 (49)
AMPC 38	Basalt	0.5	1400	15	clear	3.23	75 (4)
AMPC 25	Basalt	1.2	1400	15	part. milky	1.15	267 (12)
AMPC 39	Basalt	2	1400	15	milky	1.84	407 (19)

HPG = Haplogranite, P = pressure, T = temperature; part. milky means the glass contained both milky and clear parts. Numbers in parentheses are one standard deviation in the last digits of the measured water contents. These uncertainties include a 2.4% standard deviation in the extinction coefficient used for H_2 quantification (2.12 ± 0.05 liter $mol^{-1}cm^{-1}$), a 1% possible error each for the actual absorbance measurement and the density, an error between 0.1 and 0.3% due to a possible error of 2 µm in sample thickness (which ranged from 613 to 1546 µm). Note, however, that any systematic error due to a possible compositional dependence of the extinction coefficient is not included (see discussion in the text)

that at these temperatures, not only H_2, but also some oxygen diffuses through the wall of the inner Pt capsule. This is likely related to enhanced grain boundary diffusion upon recrystallization of the platinum at high temperature (see also Truckenbrodt and Johannes 1999 for related observations).

The efficiency of buffering at Fe-FeO-H_2O conditions in the solubility experiments depends essentially on whether the reaction of H_2O with the Fe from the outer capsule wall can keep pace with any diffusive loss of H_2. While this is difficult to directly ascertain in the experiments of the present study, the results of Vlasov et al. (2023), who used a very similar capsule design, provides strong evidence for the efficiency of the buffering technique. Vlasov et al. (2023) studied H_2-H_2O immiscibility by synthesizing aqueous fluid inclusions at Fe-FeO buffer conditions. They observed that even in runs up to 24 h duration at similar P, T conditions with similar buffer capsule design, trapped fluids consisted of roughly equal molar amounts of H_2 and H_2O, as expected for the Fe-FeO-H_2O buffer.

Infrared spectra and infrared extinction coefficients

Figure 1 shows the infrared spectra of three haplogranitic glasses produced at 1.5 GPa, 1200 ˚C and Fe-FeO-H_2O buffer with different run durations between 15 and 60 min. Aside from the OH band at 4500 cm^{-1}, they show the prominent band due to molecular H_2 in the glass near 4100 cm^{-1} (e.g. Shelby et al. 1994, Hirschman et al. 2012). The spectra and the absence of H_2 concentration profiles inside the samples suggest that equilibrium solubilities are already reached after 15 min. In fact, the spectrum from the experiments run for 60 min (APMC18) shows a slight decrease in the intensity of the 4100 cm^{-1} band as compared to the shortest run. However, in general, experiments with run durations between 15 and 270 min yielded consistent results. The first two experiments listed in Table 2 (AMPC 5 and AMPC6) that were caried out with the longest run duration (360 min) appear anomalous. Although they were caried out at the same conditions and same run duration, they yielded vastly different results in H_2 contents. The low H_2 contents observed in run AMPC5 may indicate an exhaustion of the Fe-FeO-H_2O buffer, while AMPC6 also shows an anomalously high water content that may indicate a mechanical failure of the inner capsule. These two experiments are therefore not further considered.

A detailed inspection of Fig. 1 shows a very weak band just above 5000 cm^{-1} (about 5012 cm^{-1} in haplogranite) which is distinct from the 5200 cm^{-1} band of molecular H_2O. A background-corrected version of the spectrum of sample AMPC15 from Fig. 1 is shown in Fig. 2. The same band is seen in the spectra of the glasses of haplogranitic and of MORB composition, while it is not detectable

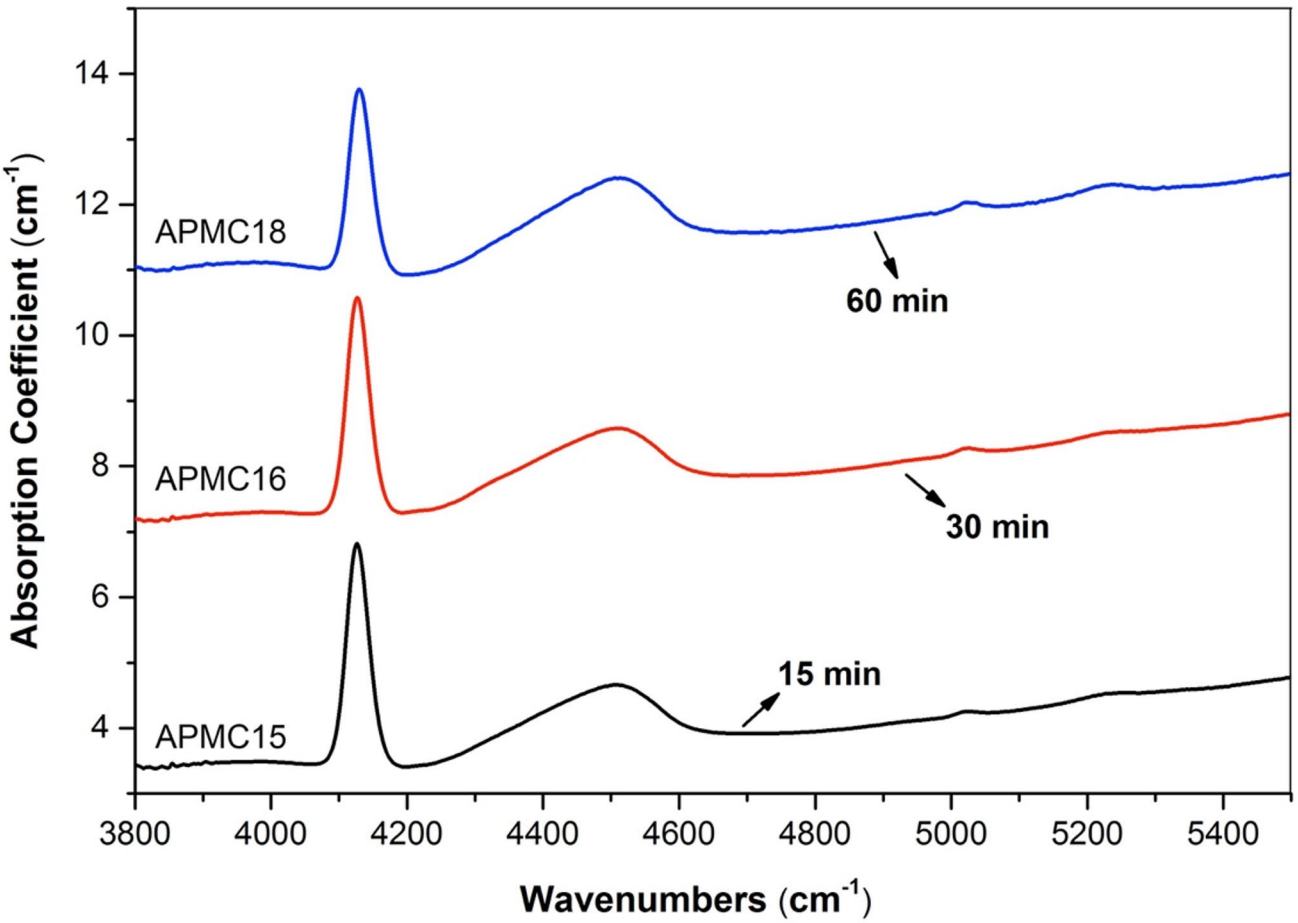

Fig. 1 Infrared spectra of three H_2-bearing haplogranitic glasses produced at 1.5 GPa, 1200 °C and Fe-FeO-H_2O buffer conditions with different run durations

in the andesitic glass samples. The intensity of this band correlates with the intensity of the 4100 cm^{-1} band of H_2 (Fig. 3). Very likely, this band is combination mode of the stretching vibration and some hindered rotation (libration) of the H_2 molecule in the glass. Indeed, Raman spectra of H_2 gas show a series of rotational bands (e.g. Schmidt et al. 1998), the highest one occurring near 1000 cm^{-1}. The precise position of the main band of H_2 near 4100 cm^{-1} shows a slight dependence on melt composition and synthesis pressure (near 4129 cm^{-1} in haplogranite, 4131 cm^{-1} in andesite). Interestingly, in Raman spectra, the same band in the same sample appears significantly narrower with the maximum shifted to higher frequency by a few wavenumbers. This may indicate that infrared and Raman spectra sample populations of H_2 molecules in different environments with somewhat different sensitivity.

A main target of the current study was the precise calibration of the infrared extinction coefficient of the 4100 cm^{-1} H_2 band. This calibration was carried out using haplogranitic glasses, as they can be easily produced already at relatively low temperatures. Two different and completely independent methods of calibration were used. In the first method, H_2-loaded glasses were first produced and their infrared spectra were measured. The glasses were then sealed with 70–80 bar high-purity (>99.999%) O_2 gas into Pt capsules and run in TZM bombs at 200 MPa and 1100 °C for 5 h, in order to oxidize any H_2 in the melt to H_2O. It should be noted that this oxidation step was carried out in a vessel with high-purity (>99.998%) Ar as pressure medium, such that no hydrogen could possibly diffuse into the capsule from the outside. After the oxidation step, the infrared spectra of the glass sample were measured again and the difference in bulk H_2O content was attributed to the H_2 that had been oxidized. Figure 4 shows an example of the infrared spectra before and after the O_2-treatment. All relevant calibration data are compiled in Table 3. In most cases, upon oxidation, the H_2O content of the sample was more than doubled, allowing a robust calibration. Moreover, in samples (TZM-45, TZM-46) that showed only a very weak H_2 band before the oxidation, the bulk water content increased, but remained very low after oxidation, which demonstrates

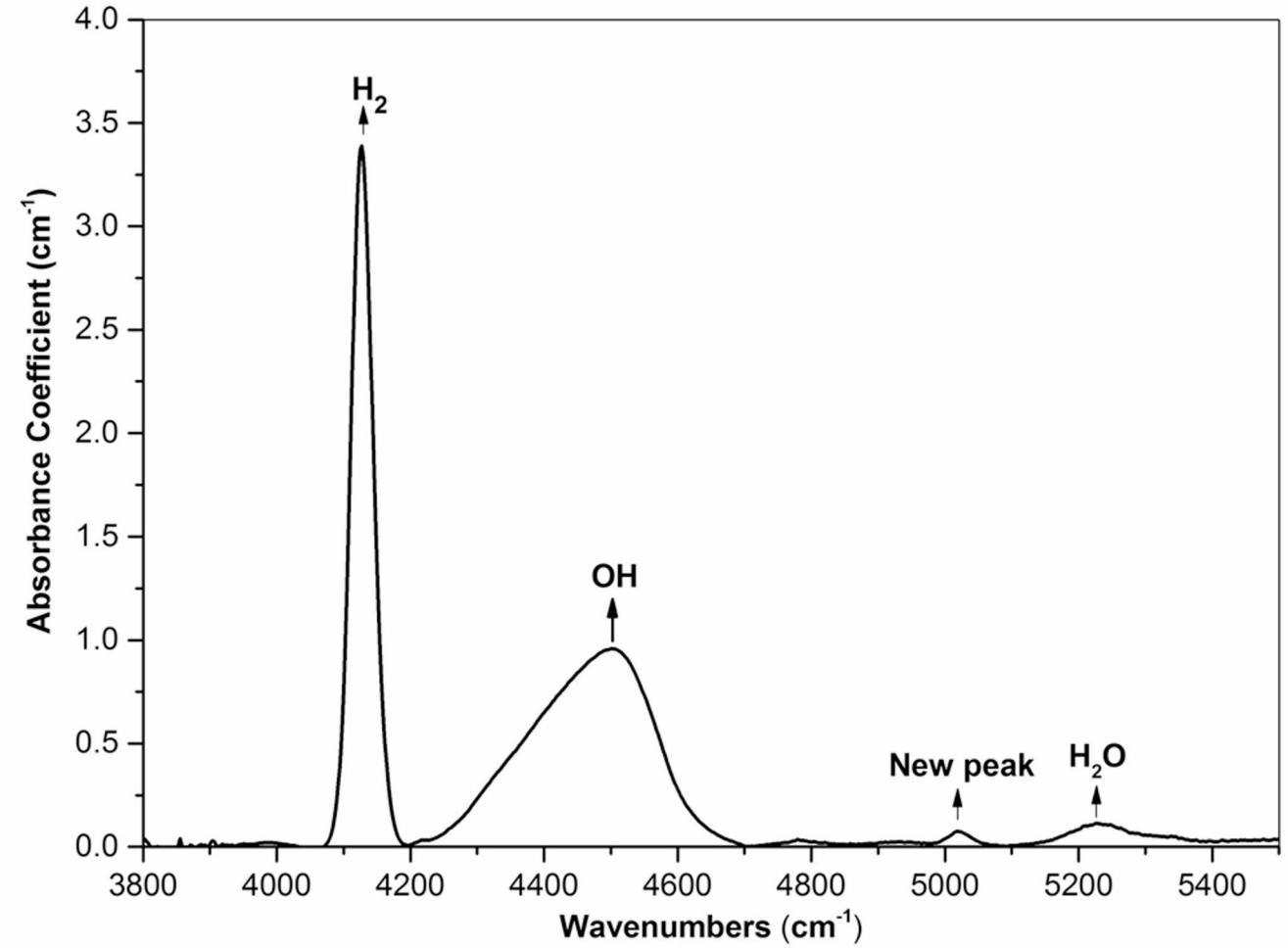

Fig. 2 Background-corrected infrared spectrum of sample AMPC15 showing the main absorption bands and the "new peak" assigned to a combination mode of molecular H_2

the absence of any H_2 diffusing into the capsule during the oxidation step.

In the second calibration method, again H_2-loaded glasses were first produced and their infrared spectra were measured in order to quantify dissolved H_2O (as OH groups and H_2O molecules). Then the total hydrogen content of these glasses was measured using Karl Fischer titration. The difference between the two measured water contents was again attributed to H_2. The relevant calibration data are compiled in Table 4. In most cases, the water content measured by Karl Fischer titration was about twice that of dissolved OH groups and H_2O as detected by infrared spectroscopy. This is due to the fact that the samples were initially prepared with CaH_2 as hydrogen source, which generates a nearly pure H_2 atmosphere without introducing water into the sample. Figure 5 compares the results from both calibration methods. The data are highly consistent and can be reproduced by one regression line passing through the origin of the diagram. The slope of this regression line is equivalent to a linear molar absorption coefficient for the 4100 cm^{-1} band of H_2 of (2.12 ± 0.05) liter $mol^{-1}cm^{-1}$. Notably, this is about one order of magnitude larger than the value reported by Shelby (1994) for H_2 in silica glass (0.26 liter $mol^{-1}cm^{-1}$). We will use this value for the quantification of H_2 in all glass samples produced in this study.

H_2 solubility in silicate melt

Already a superficial inspection of the infrared spectra of various samples shows that H_2 solubility is primarily controlled by pressure, which correlates with H_2 fugacity (Fig. 6). Figure 7 shows measured H_2 solubilities c (in ppm by weight or µg/g) as a function of pressure for the three compositions studied. The data can all be reproduced by a simple Henry style solubility law.

$$c_{H_2} = a_{\mathrm{Henry}}\, P \tag{1}$$

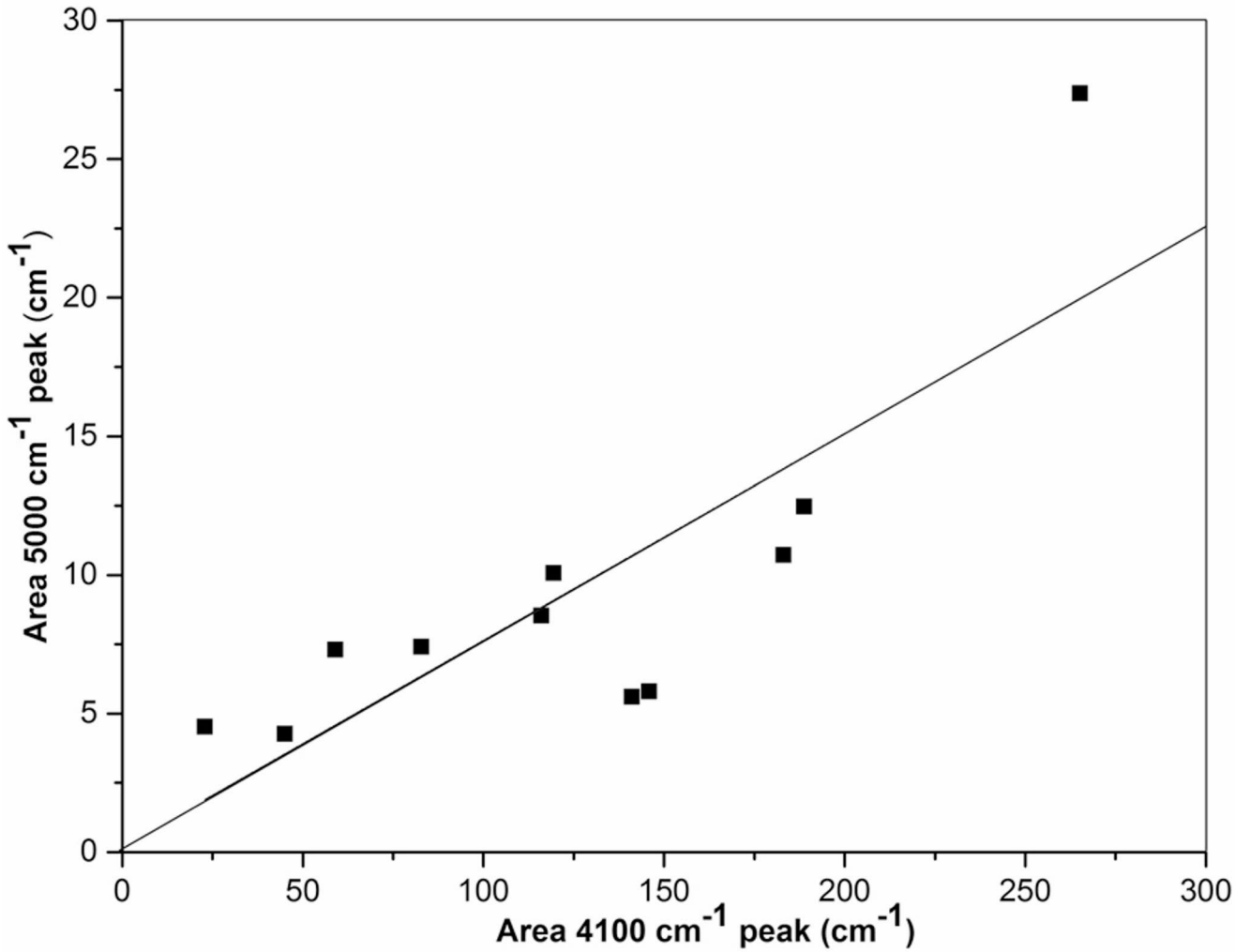

Fig. 3 Correlation between the integral intensity of the band near 5000 cm^{-1} and the main H_2 band near 4100 cm^{-1} for haplogranitic glasses

with a_{Henry} = (206 ± 10) ppm/GPa for basalt, (362 ± 35) ppm/GPa for andesite, and (500 ± 62) ppm/GPa for haplogranite. For basalt and andesite, all data are reasonably well reproduced, while for haplogranite, there are some outliers that may be related to the high viscosity of this completely polymerized melt that may have impeded equilibration. Experiments at 1200 and 1300 ˚C in the haplogranitic system did not reveal any obvious temperature dependence. The compositional dependence of H_2 solubility – with the solubility in haplogranitic melt being about 2.5 times higher than in basaltic melt – is expected from ionic porosity arguments and consistent with observations on noble gas solubilities (e.g. Carroll and Stolper 1993). For example, Schmidt and Keppler (2002) observed that the solubility of argon in haplogranitic melts is about five times larger than in a tholeiitic melt. For smaller atoms or molecules (such as H_2), this compositional effect is expected to decrease.

Discussion

Comparison to previous studies

The solubility data obtained here may be compared to the data on H_2 solubility in basaltic and andesitic melt reported by Hirschmann et al. (2012). Under comparable conditions of pressure and temperature and for the same fugacity buffer (Fe-FeO-H_2O), our data yield about one order of magnitude lower H_2 solubilities. This is, however, primarily a result of the different infrared extinction coefficients used for quantifying H_2 in the glasses. The extinction coefficient of (2.12 ± 0.05) liter $mol^{-1}cm^{-1}$ determined here is one order of magnitude larger than the coefficient of 0.26 liter $mol^{-1}cm^{-1}$ from Shelby (1994) that was used in the study of Hirschmann et al. (2012). If the data of Hirschmann et al. (2012) are re-calculated with the new extinction coefficient, they are very consistent with the current study, both

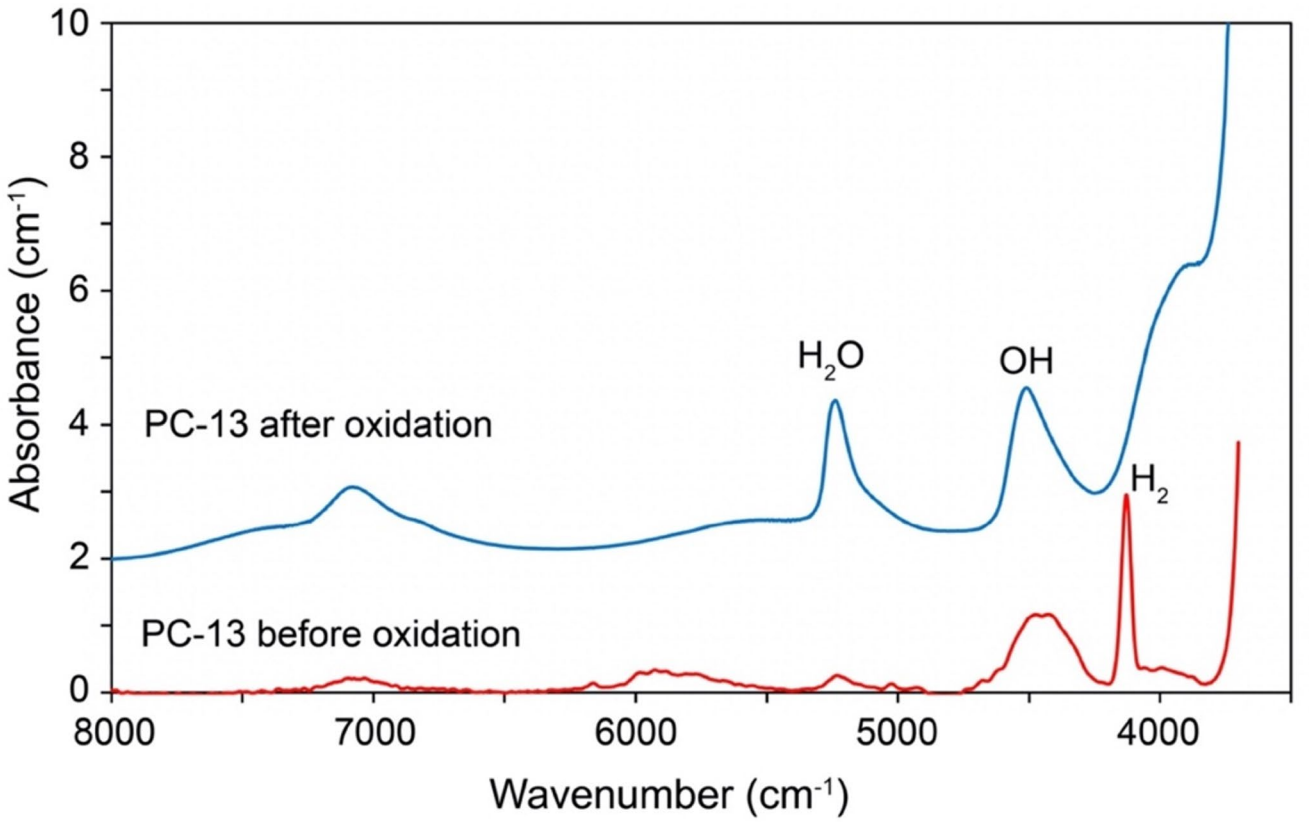

Fig. 4 Calibration of the 4100 cm^{-1} infrared band of H_2 in haplogranitic glass by oxidation with O_2. Shown are the infrared spectra of the H_2-saturated sample PC-13 before and after oxidation by treatment with O_2. The prominent H_2 band at 4100 cm^{-1} in the initial sample disappears after O_2 treatment, while the intensities of the OH band at 4500 cm^{-1} and of the H_2O band at 5200 cm^{-1} increase. The initial H_2-loaded sample contained numerous cracks due to quenching from high pressure, which somewhat reduced the quality of the spectrum

Table 3 Calibration of the H_2 extinction coefficient by treatment of the glass with pure O_2

Sample No.	*P* (GPa)	T (°C)	Duration (min)	Absorbance at 4100 cm^{-1}(cm^{-1})	Initial water content (wt%)	Oxidized water content (wt%)	Difference in water content (wt%)
PC-12	1.5	1250	5	3.10 (3)	0.733 (16)	1.776 (39)	1.04 (5)
PC-13	2	1300	5	2.82 (3)	0.764 (17)	1.849 (37)	1.08 (5)
PC-14	2	1300	2.5	3.60 (7)	0.694 (15)	1.973 (43)	1.28 (6)
PC-15	3	1350	3	2.18 (85)	0.698 (15)	1.435 (32)	0.735 (47)
TZM-45	0.15	1100	5	0.091 (1)	0.0255 (16)	0.0455 (10)	0.020 (3)
TZM-46	0.15	1100	5	0.068 (13)	0.0261 (16)	0.0336 (7)	0.0075 (23)

Pressure (P), temperature (T), and duration refer to the synthesis conditions of the initial, H_2-saturated glass. The infrared absorbance of the band at 4100 cm^{-1} due to H_2 is normalized to a sample thickness of 1 cm. Initial water content refers to the total amount of water (expressed as wt% H_2O) that was present in the initial glass as OH groups (band at 4500 cm^{-1}) and molecular water (band at 5200 cm^{-1}) according to FTIR measurements. Oxidized water content is the total amount of water that was found in the glass as OH groups and molecular water after oxidation with O_2. "Difference in water content" is the difference between "Oxidized water content" and "Initial water content", which can be attributed to the H_2 that was initially present in the glass. Numbers in parentheses give one standard deviation in the last digits of the reported value. Large uncertainties are due to inhomogeneities in the sample

in absolute values and with respect to trends in pressure and composition (Fig. 8).

As already noted in the introduction, there are two possible reasons why the extinction coefficient for silica glass by Shelby et al. (1994) may be unsuitable for quantifying H_2 in aluminosilicate glasses: (a) The extinction coefficient may be correctly determined for silica glass, but may be unsuitable for aluminosilicate glasses because it varies strongly with composition, or (b) the extinction coefficient was already incorrectly determined for silica glass due to the simple method of weight loss upon heating used to quantify hydrogen contents. Both explanations are possible, however, we consider the possibility (b) to be more likely. As noted by Ohlhorst et al. (2001), the molar extinction coefficients

Table 4 Calibration of the H_2 extinction coefficient in glass by Karl Fischer Titration (KFT)

Sample No.	*P* (GPa)	T (°C)	Duration (min)	Absorbance at 4100 cm^{-1}(cm^{-1})	Initial water content (wt%)	Total water content by KFT (wt%)	Difference in water content (wt%)
PC-5	1.5	1250	1	0.46 (22)	0.33 (1)	0.47	0.14
PC-6	2	1250	1	0.59 (20)	0.32 (1)	0.61	0.29
TZM-42	0.2	1100	5	0.024 (4)	0.037 (2)	0.084	0.047
TZM-44	0.2	1100	5	0.091 (15)	0.038 (2)	0.085	0.047

"Difference in water content" is the difference between "Total water content by KFT" and "Initial water content", which can be attributed to the H_2 that was initially present in the glass. Numbers in parentheses give one standard deviation in the last digits of the reported value. Large uncertainties are due to inhomogeneities in the sample. In the Karl Fischer titration, the entire sample was used to produce one single measurement and accordingly, no statistically meaningful error can be stated

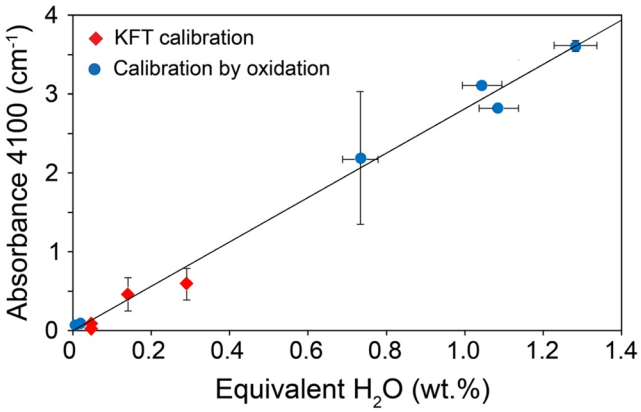

Fig. 5 Calibration of the 4100 cm^{-1} infrared band of H_2 in haplogranitic glass by Karl Fischer titration (KFT) and by oxidation with O_2. The sample with the large error bar was initially inhomogeneous. Where no error bar is shown, the uncertainty is smaller than the size of the symbol. "Equivalent H_2O" is the concentration of H_2O (in wt%) corresponding to the equal molar concentration (in mol/liter) of H_2 in the glass. The slope of the regression line shown is 2.800±0.064 (R^2=0.9977), which corresponds to an extinction coefficient of (2.12±0.05) liter $mol^{-1}cm^{-1}$

for the 4500 cm^{-1} and 5200 cm^{-1} overtone bands of OH and H_2O do change by about a factor of two from basaltic to rhyolitic compositions. For H_2, where the dipole moment responsible for interaction with infrared radiation is produced exclusively by the interaction with the matrix, even stronger dependencies are conceivable. However, in such a case, one would probably also expect major changes in the absorption frequency itself and this is not observed. Schmidt et al. (1998) observe the infrared band of H_2 in silica glass at 4138 cm^{-1}, not far away from the position in the samples studied here. On the other hand, Schmidt et al. (1998) also observed that upon interaction of H_2 with silica glass, not only H_2 is dissolved in the glass, but simultaneously also OH and silanol (Si-H) groups are formed. An OH band is also seen in the glass spectra reported by Shelby (1994). Naturally, upon heating, the hydrogen stored in these groups would also be released and contribute to the weight loss that was assigned to H_2 only by Shelby (1994). The desorption of surface adsorbed moisture and of other volatiles inside the glass may also have contributed to the weight loss. If the amount of H_2 in the sample is overestimated, the calculated infrared extinction coefficient will be underestimated and using this coefficient for H_2 quantification will cause a systematic over-estimation of actual H_2 contents.

Hirschmann et al. (2012) tried to verify the H_2 contents obtained with the infrared extinction coefficient of Shelby (1994) by using a combination of SIMS measurement of total hydrogen contents and FTIR data for dissolved OH and H_2O. H_2 contents were then obtained by subtracting the amount of hydrogen present as OH or H_2O from the measured total hydrogen. However, the correlation between these data and the H_2 contents directly inferred by infrared spectroscopy using the Shelby (1994) extinction coefficient is rather poor. Indeed, this "difference method" essentially calculates a rather small difference between two large numbers, with the effect that the uncertainties may exceed the values obtained. Also, it appears questionable whether SIMS is the optimum method to determine total hydrogen contents in glass samples that contain H_2. During the course of the present study, it was observed that mm-sized samples of H_2-loaded glass lost a significant fraction of the dissolved H_2 (up to something like 30%) when stored for several months at ambient conditions. In vacuum, such a loss may therefore rapidly occur near the surface and diffuse outgassing from the entire sample may also affect the measurements.

Since infrared extinction coefficients are certainly to some degree matrix dependent, the use of an extinction coefficient calibrated for a haplogranitic glass for determining H_2 contents of andesitic or basaltic glasses may introduce some systematic error. We argue, however, that this error cannot be very large, since the trend of H_2 solubility as a function of melt composition is quite comparable to that expected from noble gas solubility studies (Carroll and Stolper 1993; Carroll and Webster 1994). As noted above, H_2 solubility decreases from haplogranite to basalt by a factor of 2.5 (from 500 ppm/GPa to 206 ppm/GPa). Noble gas studies also generally show a decrease of solubility in the same direction, with the effect of melt composition being

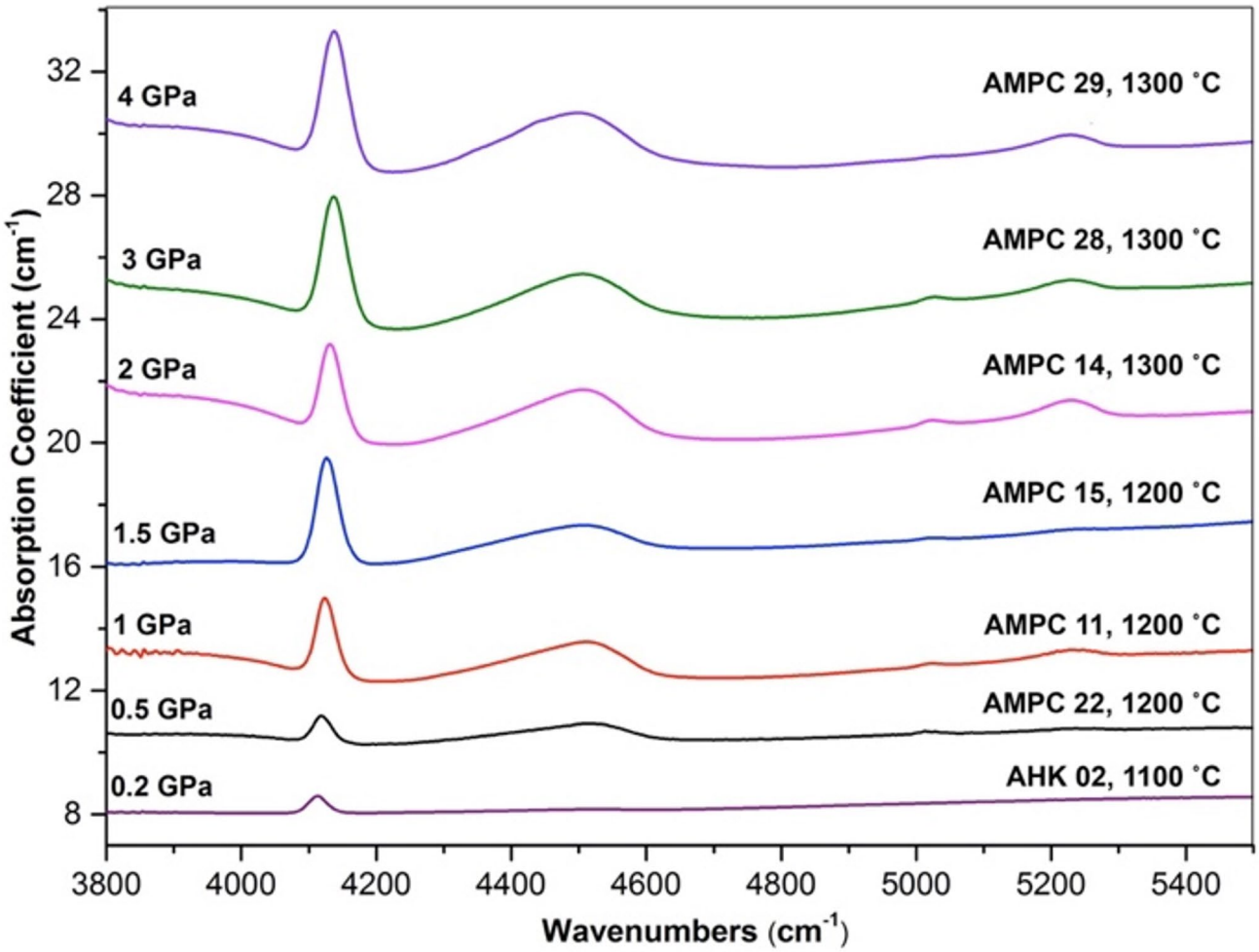

Fig. 6 Effect of pressure on H_2 solubility in haplogranitic melt, as seen in the infrared spectra. Sample AHK02 was equilibrated with pure H_2 gas, the others were in equilibrium with the Fe-FeO-H_2O buffer

larger for the heavy noble gases than for the lighter noble gases. This likely reflects the different size of the atoms fitting into the silicate network of the melt, with larger atoms experiencing a stronger effect of melt composition on solubility. Comparing the size of a diatomic molecule like H_2 to the size of a spherical noble gas atom is difficult, but the molar volume of the pure liquid may serve as a rough guide. The molar volume of liquid H_2 at its boiling point (20 K) is 32.0 cm^3/mol, similar to that of helium at its boiling point (28.2 cm^3/mol at 4 K). Similarly, the collision cross section of H_2 is slightly above that of helium (0.27 nm^2 versus 0.21 nm^2, Atkins 1982). For helium, the solubilities in rhyolitic and MORB melt differ by about a factor of two (Carroll and Webster 1994), very close to the factor of 2.5 observed here for H_2. Moreover, for N_2, which is somewhat larger than H_2, a difference by a factor of 3.2 is observed (Keppler et al. 2022). These observations suggest that the differences in H_2 solubility as a function of composition observed here are plausible and the quantification using the extinction coefficient calibrated for haplogranitic glass is reliable. Any major compositional dependence of the infrared extinction coefficient would have caused trends in H_2 solubility as function of melt composition deviating from that expected from the He and N_2 data.

Thermodynamics of H_2 solubility in silicate melts

As noted above, the measured H_2 solubilities at Fe-FeO buffer condition can be conveniently described by a simple Henry-style solubility law, where H_2 in the melt is directly proportional to total gas pressure. This is consistent with the empirical observation made in many gas-silicate melt systems that solubility of molecular or atomic gases scales linearly with pressure up to the GPa pressure range. Examples include CO_2 (Ni and Keppler 2013 and references therein), N_2 (Keppler et al. 2022), and noble gases (Schmidt and Keppler 2002). Ar solubility deviates from direct proportionality to gas pressure only above 3 GPa (Schmidt and Keppler

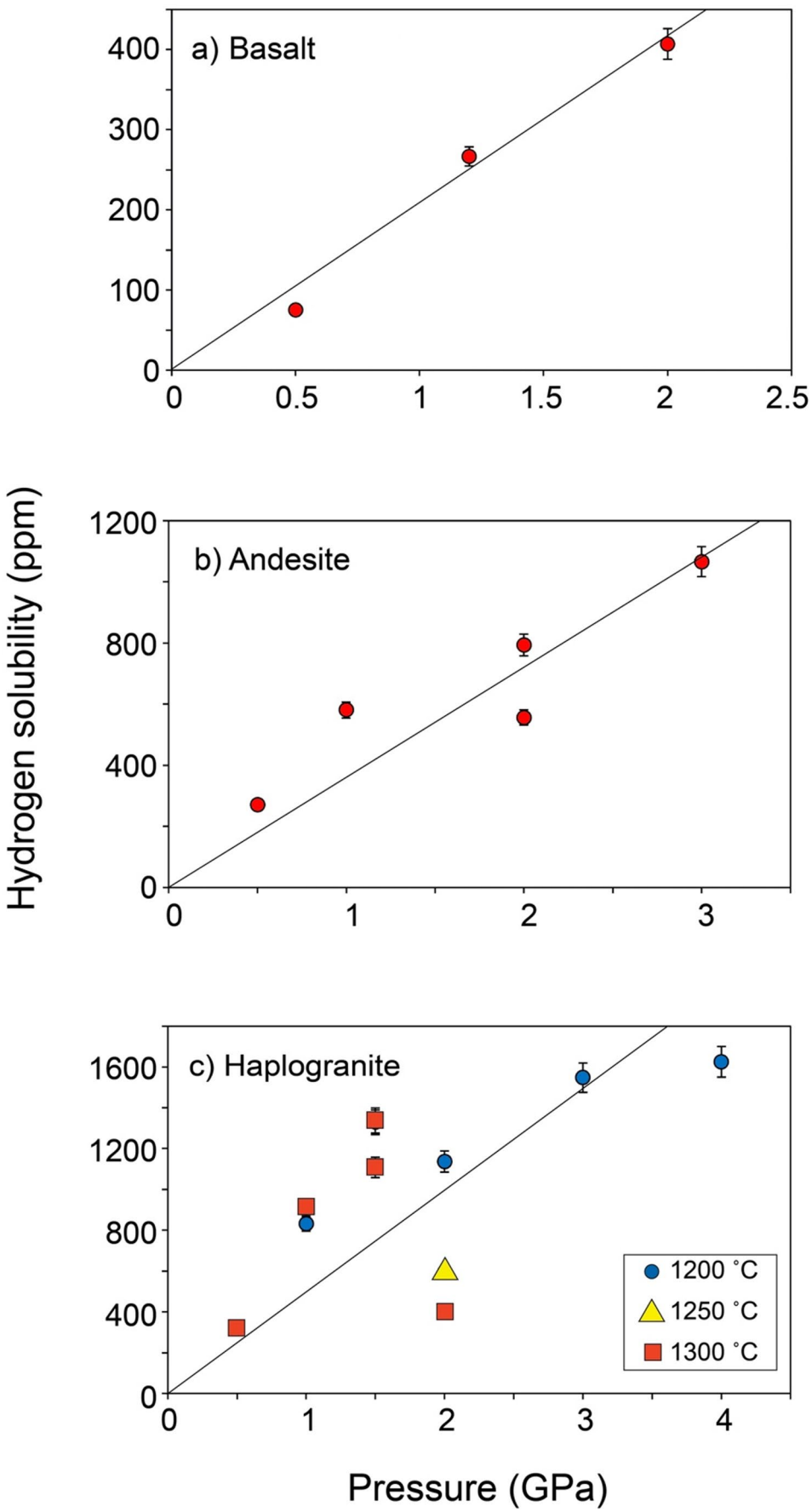

Fig. 7 H_2 solubility in basaltic, andesitic, and haplogranitic melt at Fe-FeO-H_2O buffer conditions as a function of pressure. The basalt and andesite experiments were all carried out at 1400 ˚C. Shown are also linear regression curves for all data of the form $c_{H2} = a_{Henry}$ P, with a_{Henry} = (206 ± 10) ppm/GPa for basalt, (362 ± 35) ppm/GPa for andesite, and (500 ± 62) ppm/GPa for haplogranite. For the definition of the error bars see Table 2

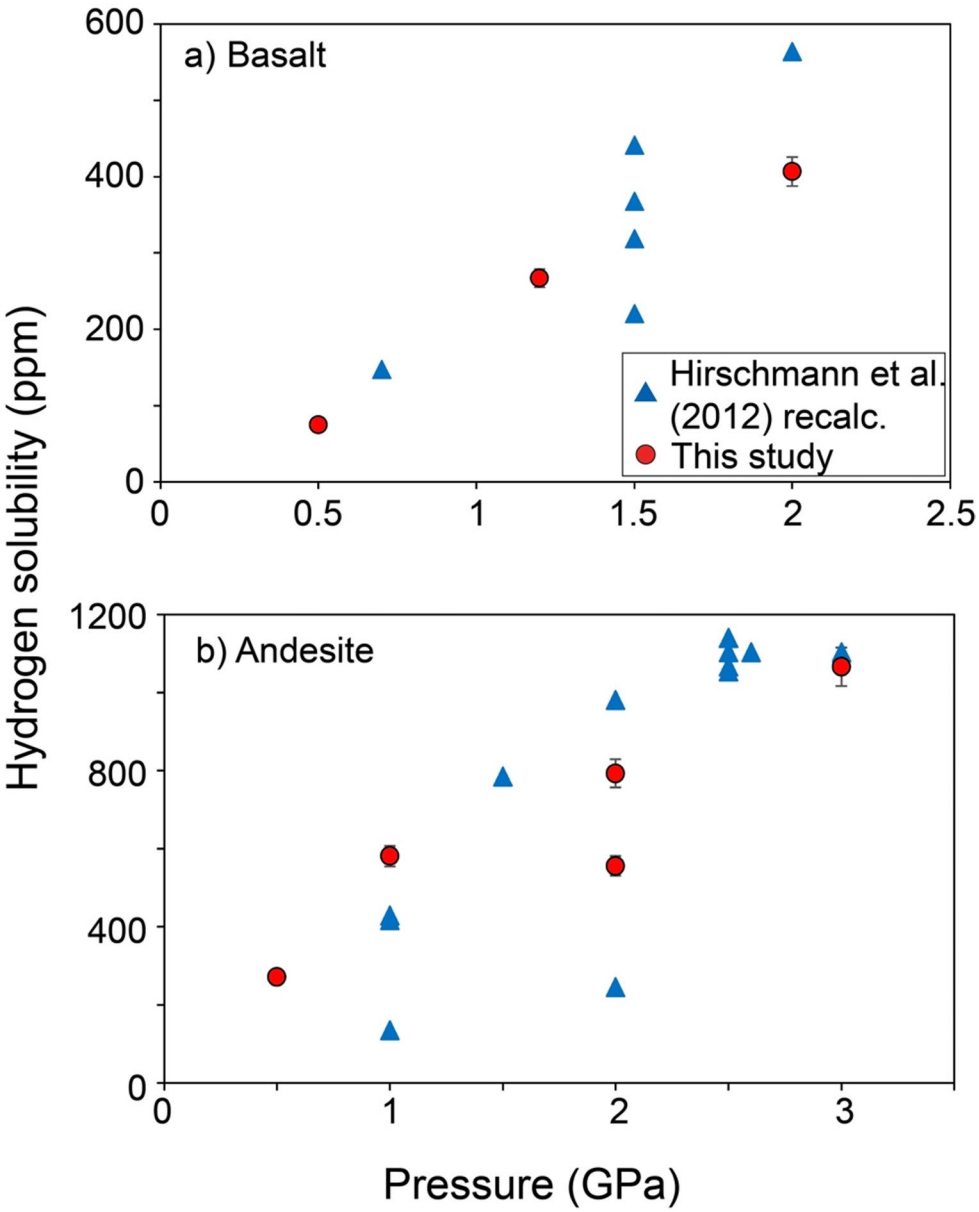

Fig. 8 Comparison of the results of the current study with that of Hirschmann et al. (2012) on H_2 solubility in basaltic and andesitic melt as a function of pressure. Only experiments caried out at Fe-FeO-H_2O buffer conditions are shown. The data from Hirschmann et al. (2012) are recalculated using the infrared extinction coefficient obtained in the current study, which reduces the values by one order of magnitude as compared to those previously reported. The basalt and andesite experiments of the current study were all performed at 1400˚C, like most of those of Hirschmann et al. (2012). The latter dataset also includes two basalt experiments at 1450 ˚C and two andesite experiments at 1500 ˚C. For the definition of the error bars see Table 2. No estimates of error are available for the original solubility data of Hirschmann et al. (2012)

2002). N_2 solubility shows perfect Henry law behavior to at least 2 GPa (Keppler et al. 2022). The only notable exception from this rule is water, which largely dissociates into OH groups in the melt, such that solubility in first approximation is proportional to the square root of water fugacity (e.g., Shishkina et al. 2010; Putak Juriček and Keppler 2024).

As an alternative to the Henry-style solubility model, particularly for high pressures > 1 GPa, we also develop here a more general thermodynamic solubility model for H_2. This is based on the solubility reaction:

$$H_2\,(\text{gas}) = H_2\,(\text{melt}) \tag{2}$$

with the equilibrium constant

$$K = \frac{a_{H_2}^{melt}}{f_{H_2}^{gas}} \tag{3}$$

with $a_{H_2}^{melt}$ being the activity of H_2 in the silicate melt, and $f_{H_2}^{gas}$ being the fugacity of H_2 in the gas phase. The equilibrium constant is related to change in Gibbs free energy ΔG during the reaction through.

$$-\text{RTln K} = -\text{RT ln}\,\frac{a_{H_2}^{melt}}{f_{H_2}^{gas}} = \Delta\text{G} = \Delta\text{H} - \text{T}\Delta\text{S} + \text{P}\Delta\text{V} \tag{4}$$

where ΔH and ΔS are the enthalpy and entropy changes upon dissolution of H_2 from the gas phase into the melt and ΔV is the volume change of the melt phase upon dissolution of H_2. The intrinsic temperature dependence of gas solubilities in silicate melts is often rather small (see, e.g. Ni and Keppler

2013 for CO_2) and the experimental data obtained here are not sufficient to resolve such a temperature dependence. Therefore, the ΔH-TΔS term in the above equation may be treated as one single constant. Moreover, we approximate $a_{H_2}^{melt}$ by the concentration c of H_2 in the melt (in ppm by weight). With these simplifications, the above equation may be re-written as.

$$\ln \frac{c_{H_2}^{melt}}{f_{H_2}^{gas}} = \mathrm{a} + \mathrm{b}\ \mathrm{P} \tag{5}$$

with b = -ΔV/RT. A corresponding plot of $\frac{c_{H_2}^{melt}}{f_{H_2}^{gas}}$ versus pressure is shown in Fig. 9, yielding the regression parameters a = −3.675 ± 0.277, b = −0.371 ± 0.201 for basalt (R^2 = 0.77), a = −2.250 ± 0.232, b = −0.801 ± 0.121 for andesite (R^2 = 0.94), and a = −1.930 ± 0.362, b = −0.811 ± 0.184 for haplogranite (R^2 = 0.64). The fit parameters b may be converted to ΔV, the volume change of the melt upon dissolution

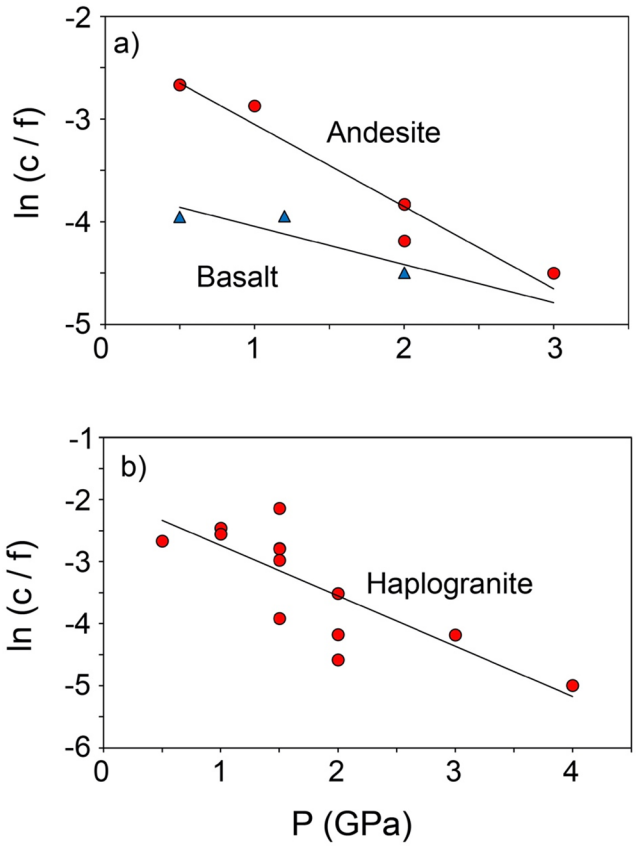

Fig. 9 Thermodynamic treatment of H_2 solubility in silicate melts. Shown is a plot of ln(c/f) versus pressure, where c is H_2 concentration in the melt in ppm by weight and f is hydrogen fugacity. The data for basalt and andesite are for 1400 ˚C, the haplogranite data for 1200 to 1300 ˚C. Errors due to analytical uncertainties in c are smaller than the symbols shown, but errors due to possible incomplete equilibration cannot be quantified. The regression lines shown have the form ln(c/f) = a + b P, with a = −3.675, b = −0.371 for basalt, a = −2.250, b = −0.801 for andesite, and a = −1.930, b = −0.811 for haplogranite

of H_2. This yields values of 10.3 cm^3/mol for haplogranite and 11.1 cm^3/mol for andesite. The latter value agrees very well with ΔV = 11.3 cm^3/mol reported by Hirschmann et al. (2012). Here, it is important to note that the value of ΔV only depends on the relative solubility changes with pressure, it is insensitive to the absolute value of solubility and therefore, insensitive to the extinction coefficient used to evaluate the FTIR data. For basalt, we obtain ΔV of 5.2 cm^3/mol, which appears anomalously low if compared to the other melt compositions and it also disagrees with the value of 10.6 cm^3/mol reported for basalt by Hirschmann (2012). This may, however, be an artifact of the rather small pressure range of the basalt data covered in our study. We therefore do not recommend using these parameters to extrapolate the solubility data of basalt beyond the measured range.

The thermodynamic solubility law for hydrogen according to Eq. (5) is particularly useful for calculating H_2 solubility in the GPa pressure range. For lower pressures, however, the Henry-style solubility law according to Eq. (1) is easier to use and probably also more accurate. The Henry-style solubility coefficients reported here (a_{Henry} = 206 ppm/GPa for basalt, 362 ppm/GPa for andesite, and 500 ppm/GPa for haplogranite) were experimentally determined for Fe-FeO buffer conditions. For different buffers or for pure hydrogen, they need to be adjusted proportionally to the expected water activity in the coexisting fluid phase.

Hydrogen dissolution in a magma ocean

Earth and the other terrestrial planets most likely formed by the accretion of chondritic material. Most models assume a mixture of ordinary chondrites with a small fraction of volatile-rich carbonaceous chondrites (e.g., Rubie et al. 2015; Alexander 2017), while a significant or even dominant contribution of volatile-poor enstatite chondrites has also been suggested (Piani et al. 2020). Heating by large impacts and by radioactive decay almost certainly caused widespread melting of the early planets, with a magma ocean coexisting with a primordial atmosphere (e.g. Elkins-Tanton 2008, 2012; Rubie et al. 2011, 2015). The chemical equilibrium between this magma ocean and the primordial atmosphere likely controlled the initial volatile distribution in planetary interiors. During solidification of the magma ocean, degassing may have produced a secondary atmosphere and oceans (e.g., Elkins-Tanton 2008; Gaillard et al. 2022), while the primordial atmosphere may have been largely lost by processes such as hydrodynamic escape (Johnstone et al. 2019; Katyal 2020) and impact erosion (Walker 1986). Since chondritic material contains metallic iron, these processes must have happened under rather reducing conditions, plausibly two log units or more below the Fe-FeO buffer (Rubie et al. 2011, 2015). Under these conditions, a

large fraction of the H_2O in the primordial atmosphere may have been reduced to H_2 (e.g., Gaillard et al. 2022). Accordingly, it has been suggested that the dissolution of H_2 in the magma ocean may have set the initial hydrogen abundance in the terrestrial planets, possibly also by capturing some H_2 from nebular gas (e.g., Young et al. 2023). With the newly calibrated solubility data from this study, this hypothesis may be tested.

For illustration and as a useful endmember, we discuss a very simple model. We assume that the Earth accreted either from ordinary chondrites or from a mixture of ordinary chondrites with a small fraction of carbonaceous chondrite material added. We then assume that the system remained initially closed, such that all the water or hydrogen present in the early planet partitioned between the magma ocean and the primordial atmosphere. This provides some upper limit of the amount of hydrogen or water that may have been dissolved in the primordial mantle. In reality, a large fraction of the primordial atmosphere may have been lost at some time due to impact erosion and hydrodynamic escape. For ordinary chondrites, we assume a bulk hydrogen content of 0.12 wt% H (Alexander et al. 2018). Hydrogen contents in carbonaceous chondrites are rather variable. Here, we assume the value of 1.55 wt% H for the most hydrogen-rich CI chondrites (Alexander et al. 2018). This is not far away from the averaged carbonaceous chondrite value of $6.60 \cdot 10^{-3}$ mol H_2O/g suggested by Marty (2012), which would translate into 1.32 wt% H. Atmospheric pressure can be calculated from the equation $P = m_{gas} \cdot g / A$, where m_{gas} is the mass of the gas atmosphere, g is gravitational acceleration and A is the surface of the planet. A and g are assumed to be the same as on the modern Earth, a first estimate of m_{gas} can be obtained by multiplying the mass of the current Earth with the mass fraction of H (or of H_2O for an H_2O atmosphere) in the chondritic material. This initial estimate then needs to be re-adjusted to account for the dissolution of some of the gas in the magma ocean.

In a simple model calculation, we assume equilibrium between the magma ocean and an atmosphere, with a bulk composition equivalent to ordinary chondrites or a mixture of ordinary chondrite with a small amount of carbonaceous chondrite material. In a first version of the model, it is further assumed that oxygen fugacity is so low that all H_2O has been reduced to H_2. For a purely chondritic composition, this model yields an atmospheric pressure of 138 MPa, if all H_2 were present in the atmosphere. Using the H_2 solubility law at Fe-FeO buffer conditions derived here for basalt (206 ppm/GPa), hydrogen solubility in the melt in equilibrium with a pure H_2 atmosphere can be estimated. At the experimentally calibrated conditions (0.5–2 GPa, 1400 ˚C), the fluid phase coexisting with the Fe-FeO buffer consists of about 46 to 32 mol % of H_2 at 0.5 to 2 GPa (calculated assuming ideal mixing of real gases). If one assumes further that H_2 solubility in the silicate melt is proportional to H_2 fugacity, this would imply a H_2 solubility of about 515 ppm/GPa in the presence of a pure H_2 atmosphere. After full equilibration between magma ocean and atmosphere, the atmospheric pressure decreases to 133 MPa in equilibrium with 68 ppm H_2 in the magma ocean. Allowing for 5% of CI chondrite material in the bulk composition (the remaining 95% being ordinary chondrite) the values are 212 MPa and 109 ppm H_2. If converted to the more common ppm by weight of H_2O, the hydrogen concentrations in the magma ocean for the two cases considered would correspond to initial abundances in the un-degassed bulk mantle of 612 ppm and 981 ppm H_2O or 1.8 to 2.9 ocean masses. These numbers are far lower than the 10 ± 5 ocean masses obtained by Marty (2012) from ^{40}Ar abundances and estimates of (mostly upper mantle) volatile element ratios. However, they appear to be in a plausible range if compared to current estimates of bulk Earth water contents that are based on direct observations of water abundances in mantle xenoliths and water contents in primitive MORB and OIB magmas (e.g., Michael 1988, 1995; Danyushevsky et al. 2000; Saal et al. 2002). For the depleted upper mantle, they yield typically water concentrations in the 100 to 300 ppm range (e.g. Hirschmann 2018). If the oceans formed by degassing of the primitive mantle, another 350 ppm (one ocean mass distributed throughout the entire mantle) would have to be added to these values, which brings them close to the values inferred from the equilibrium between a magma ocean and a dense H_2 atmosphere. The main uncertainty in all these calculations is the poorly constrained bulk abundance of water in the transition zone and the lower mantle of the Earth. A major water enrichment in the transition zone alone could easily create a water reservoir exceeding one ocean mass.

While the simple model calculations shown above may suggest that in principle, Earth´s initial water reservoir could have been created by H_2 dissolving in a magma ocean, we consider this to be unlikely, for the following reasons: (1) We estimated H_2 solubility in the magma ocean using solubility data obtained for a basaltic melt at 1400 ˚C, while the magma ocean had peridotitic compositions and temperatures near or above 2000 ˚C. Noble gas solubility data, however, suggest that also H_2 solubility should be in a peridotitic melt much lower than in a basaltic melt (Carroll and Stolper 1993; Carroll and Webster 1994). As noted above, the compositional dependence of H_2 solubility appears to be similar to or slightly larger than that observed for He. Already for He, solubility in komatiite melt is by nearly a factor of two lower than for MORB melt and for a peridotite melt, this difference should be even larger. Considering this compositional effect, the predicted H_2 solubilities in a magma ocean would have difficulties to produce

the water inventory in the modern Earth. (2) The assumption of closed-system behavior in a magma ocean – reduced primordial atmosphere system is unrealistic, as certainly massive atmospheric loss by both hydrodynamic escape (Johnstone et al. 2019; Katyal 2020) and by impact erosion (Walker 1986) must have occurred.

For the two reasons outlined above, it appears rather unlikely that dissolution of H_2 in the magma ocean is the main source of hydrogen on the Earth or on other terrestrial planets. However, if conditions are sufficiently oxidizing to convert some of the H_2 in the primordial atmosphere into H_2O, high water inventories in the magma ocean are easily achieved. This is not only due to the intrinsically much higher solubility of water in the silicate melt (e.g., Dixon et al. 1995; Shishkina et al. 2010; Putak Juricek et al. 2024 for basaltic melt, Sossi et al. 2023 for peridotitic melt), but also due to another effect: The mass of the H_2O molecule is larger than that of H_2, which translates into a proportional increase in atmospheric pressure by about one order of magnitude, if all H_2 is converted to H_2O. After considering the hypothetical case of a pure H_2 atmosphere coexisting with a magma ocean, we therefore now discuss the case for a mixed H_2-H_2O atmosphere, where the H_2/H_2O ratio is controlled by the oxygen fugacity. The primary control of oxygen fugacity in the early magma ocean-atmosphere system is the equilibrium between metallic iron and the FeO component in the silicate melt. For the final stages of accretion, this yields plausible values of oxygen fugacity two log units below the iron wüstite buffer (log fO_2 = IW-2). However, for earlier stages of accretion, even more reducing conditions down to IW-4 or below may have been possible (Rubie et al. 2011). In Fig. 10, we show the distribution of hydrogen – as H_2 or H_2O – between a primordial atmosphere and a magma ocean at 2000 ˚C, assuming a chondritic bulk composition (95% ordinary chondrite, 5% carbonaceous chondrite) and closed-system behavior. Oxygen fugacity at the Fe-FeO buffer was calculated by extrapolating the data of Eugster and Wones (1962) to higher temperatures. The equilibrium constant for the reaction $H_2 + ½\ O_2 = H_2O$ is from Robie and Hemingway (1995), assuming ideal mixing in the gas phase. Hydrogen solubility in the melt is assumed to be 515 ppm H_2/GPa (see above) and for H_2O solubility in the melt, we assume the model reported by Shishkina et al. (2010) for basaltic melt ($c_{H_2O} = 0.2351\ P^{0.5758}$, where c_{H_2O} is water concentration in the melt in wt% and P is H_2O partial pressure in MPa).

The equilibrium distribution of H_2 and H_2O between magma ocean and primordial atmosphere was calculated by solving the following mass balance:

$$m_{H_2}^{gas} + m_{H_2}^{melt} + m_{H_2O}^{gas} + m_{H_2O}^{melt} = m_{H_2O}^{total} \quad (6)$$

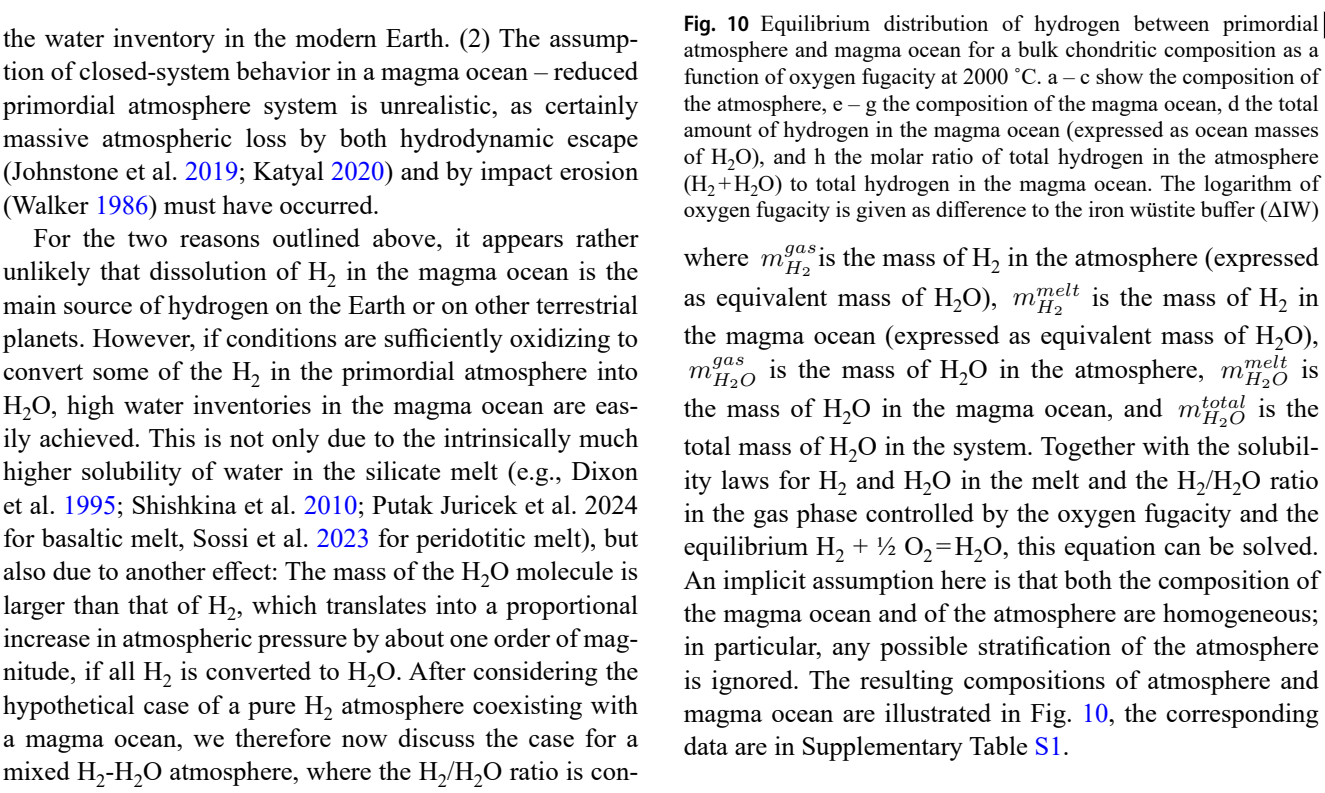

Fig. 10 Equilibrium distribution of hydrogen between primordial atmosphere and magma ocean for a bulk chondritic composition as a function of oxygen fugacity at 2000 ˚C. a – c show the composition of the atmosphere, e – g the composition of the magma ocean, d the total amount of hydrogen in the magma ocean (expressed as ocean masses of H_2O), and h the molar ratio of total hydrogen in the atmosphere (H_2+H_2O) to total hydrogen in the magma ocean. The logarithm of oxygen fugacity is given as difference to the iron wüstite buffer (ΔIW)

where $m_{H_2}^{gas}$ is the mass of H_2 in the atmosphere (expressed as equivalent mass of H_2O), $m_{H_2}^{melt}$ is the mass of H_2 in the magma ocean (expressed as equivalent mass of H_2O), $m_{H_2O}^{gas}$ is the mass of H_2O in the atmosphere, $m_{H_2O}^{melt}$ is the mass of H_2O in the magma ocean, and $m_{H_2O}^{total}$ is the total mass of H_2O in the system. Together with the solubility laws for H_2 and H_2O in the melt and the H_2/H_2O ratio in the gas phase controlled by the oxygen fugacity and the equilibrium $H_2 + ½\ O_2 = H_2O$, this equation can be solved. An implicit assumption here is that both the composition of the magma ocean and of the atmosphere are homogeneous; in particular, any possible stratification of the atmosphere is ignored. The resulting compositions of atmosphere and magma ocean are illustrated in Fig. 10, the corresponding data are in Supplementary Table S1.

The following observations can be made from the data shown in Fig. 10:

(1) Under the most reducing conditions considered (log fO_2 = IW-6), a H_2-dominated atmosphere with a total pressure of about 205 MPa coexists with a magma ocean (Fig. 10a-c). Nevertheless, even under these conditions, the hydrogen budget of the magma ocean is dominated by dissolved water, with a molar ratio of H_2/H_2O below unity (Fig. 10e-g). The redox condition of IW-6 is far below that assumed for the terrestrial magma ocean (Rubie et al. 2011). This clearly shows that under plausible conditions, dissolved H_2 will never dominate the hydrogen budget in a terrestrial magma ocean or in the early Earth´s mantle after solidification of the magma ocean.

(2) For plausible redox conditions of the terrestrial magma ocean near the end of accretion (log fO_2 near IW-2, Rubie et al. 2011), only 6 mol % of the hydrogen in the magma ocean is dissolved as H_2, with 94% being H_2O (Fig. 10g). The total amount of hydrogen (H_2+H_2O) in the magma ocean would be equivalent to 40 ocean masses.

(3) Although converting H_2 into H_2O increases atmospheric mass and therefore atmospheric pressure by a factor of 9 for a constant hydrogen inventory in the atmosphere, bulk atmospheric pressure actually decreases with increasing oxygen fugacity. This is due to the much higher solubility of H_2O in the magma ocean as compared to H_2 (see also Sossi et al. 2023).

(4) If earlier stages of accretion occurred under highly reducing conditions near IW-4, hydrogen loss due to

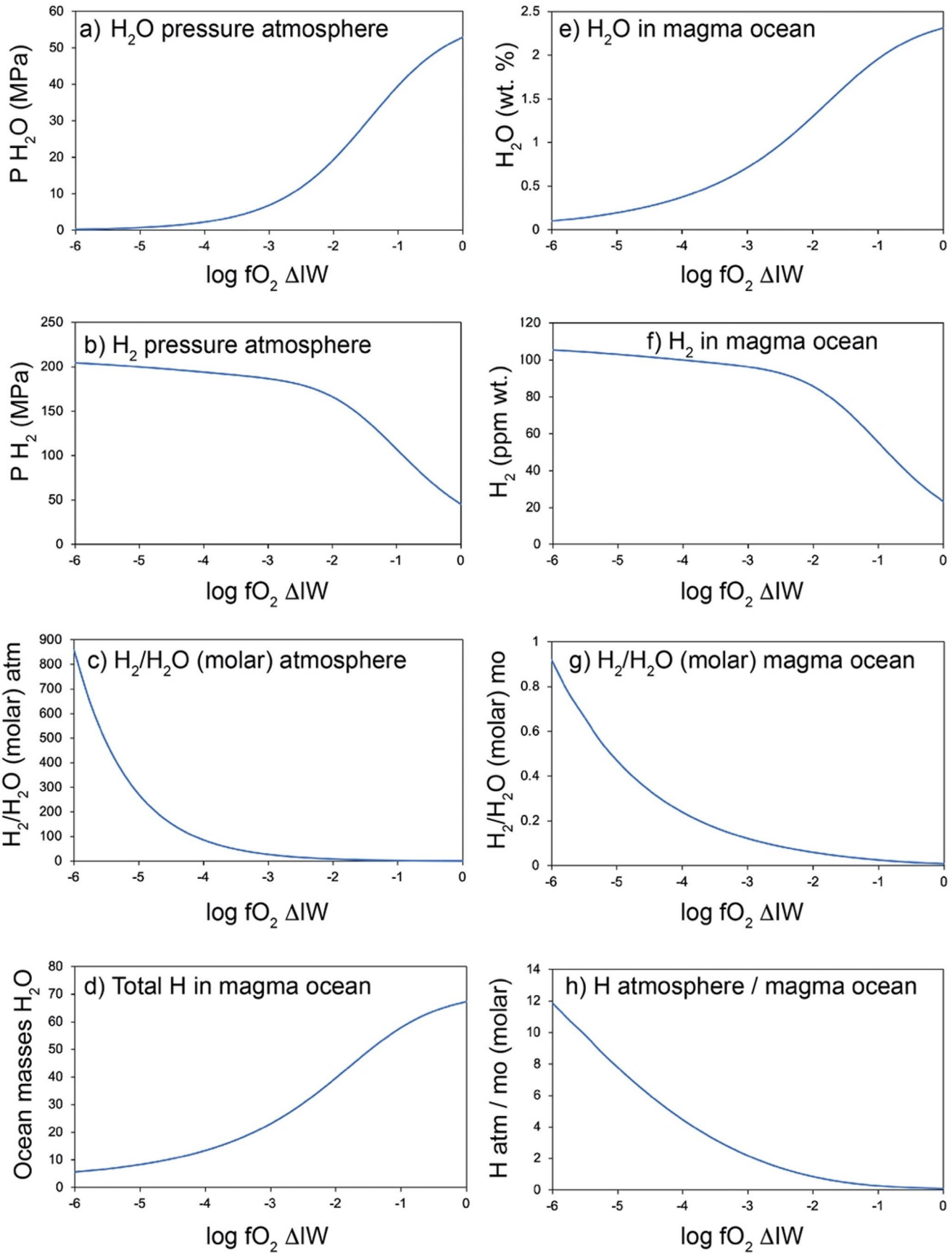
a) H_2O pressure atmosphere
P H_2O (MPa)
log fO_2 ΔIW
e) H_2O in magma ocean
H_2O (wt. %)
log fO_2 ΔIW
b) H_2 pressure atmosphere
P H_2 (MPa)
log fO_2 ΔIW
f) H_2 in magma ocean
H_2 (ppm wt.)
log fO_2 ΔIW
c) H_2/H_2O (molar) atmosphere
H_2/H_2O (molar) atm
log fO_2 ΔIW
g) H_2/H_2O (molar) magma ocean
H_2/H_2O (molar) mo
log fO_2 ΔIW
d) Total H in magma ocean
Ocean masses H_2O
log fO_2 ΔIW
h) H atmosphere / magma ocean
H atm / mo (molar)
log fO_2 ΔIW

hydrodynamic escape and impact erosion would have been favored by the high H_2 partial pressures and by the fact that the majority of the terrestrial hydrogen reservoir resided in the atmosphere (Fig. 10h).

Molecular hydrogen is therefore unlikely to be a major source of the volatile inventory in Earth´s early mantle. However, the conversion of H_2O to H_2 at low oxygen fugacities may have enhanced hydrodynamic escape during early stages of the magma ocean. Hydrodynamic escape or impact losses are required in order to achieve the current hydrogen inventory of the Earth, as simple equilibration in a closed atmosphere-magma ocean system would predict unreasonably high water inventories in the primitive mantle. These losses may have been enhanced if during early accretion under very reducing conditions, most of the hydrogen partitioned into the atmosphere.

In the model described above, the presence of volatiles other than hydrogen, notably carbon, has been ignored. Indeed, the presence of carbon would have virtually no effect on the atmospheric pressures and solubilities of H_2 and H_2O, because methane CH_4 is the only relevant C-H compound in this system. Methane, however, is only a very minor species in the gas phase at the relevant high temperatures and moderate pressures (e.g., Gaillard et al. 2022). Because of the high solubility of H_2O in the silicate melt, CO and CO_2 may dominate the atmospheric composition at oxygen fugacities higher than 4 log units below the iron wüstite buffer (e.g., Gaillard et al. 2022; Sossi et al. 2023). This, however, also depends on the assumed bulk volatile abundances in the system. The possible maximal partial pressures of CO and CO_2 are limited by graphite saturation (e.g., Golabek and Keppler 2019), while no such limit exists for H_2O partial pressures. For this reason, high bulk abundances of volatiles, like in the chondritic model discussed here, may favor atmospheres that are dominated by H_2 and H_2O.

Conclusions

We have re-calibrated the infrared extinction coefficient of H_2 in silicate glasses. The coefficient that was previously used for quantifying H_2 solubility in silicate melt was probably underestimated by about one order of magnitude, implying that previous studies overestimated H_2 solubility in melts by the same factor. However, if the data are corrected with the proper extinction coefficient, they agree very well with our study. In the light of the new solubility calibration, it appears very unlikely that the dissolution of H_2 in the magma ocean has made a major contribution to the volatile inventory of the early Earth. Quite to the contrary, the main effect of stabilizing H_2 at low oxygen fugacities appears to be that hydrogen strongly partitions into the atmosphere, which favors volatile loss by hydrodynamic escape and impact erosion.

Supplementary Information The online version contains supplementary material available at https://doi.org/10.1007/s00410-025-02272-y.

Acknowledgements The authors like to thank Hubert Schulze and Raphael Njul for sample cutting and polishing and Detlef Krauße for assistance with electron microprobe analyses. Very constructive reviews by Fabrice Gaillard and Paolo Sossi, as well as swift editorial handling by Dante Canil are highly appreciated.

Author contributions Alok Chaudhari carried out all the H_2 solubility experiments, analyzed the run products and did a first data analysis with guidance and assistance by Matteo Masotta and Svyatoslav Shcheka. Hans Keppler carried out and evaluated all experiments related to the calibration of the H_2 infrared extinction coefficient. Hans Keppler designed this study and wrote the first draft of the manuscript, with corrections and improvements by all coauthors.

Funding Open Access funding enabled and organized by Projekt DEAL.

Open Access This article is licensed under a Creative Commons Attribution 4.0 International License, which permits use, sharing, adaptation, distribution and reproduction in any medium or format, as long as you give appropriate credit to the original author(s) and the source, provide a link to the Creative Commons licence, and indicate if changes were made. The images or other third party material in this article are included in the article's Creative Commons licence, unless indicated otherwise in a credit line to the material. If material is not included in the article's Creative Commons licence and your intended use is not permitted by statutory regulation or exceeds the permitted use, you will need to obtain permission directly from the copyright holder. To view a copy of this licence, visit http://creativecommons.org/licenses/by/4.0/.

References

Alexander CMOD (2017) The origin of inner solar system water. Phil Trans R Soc A 375:20150384

Alexander CMOD, McKeegan KD, Altwegg K (2018) Water reservoirs in small planetary bodies: Meteorites, asteroids, and comets. Space Sci Rev 214:36

Atkins PW (1982) Physical chemistry, 2nd edn. Oxford University Press

Behrens H, Romano C, Nowak M, Holtz F, Dingwell DB (1996) Near-infrared spectroscopic determination of water species in glasses of the system $MAlSi_3O_8$ (M = Li, Na, K): an interlaboratory study. Chem Geol 128:41–63

Boettcher SL, Guo Q, Montana A (1989) A simple device for loading gases in high pressure experiments. Am Mineral 74:1383–1384

Carroll MR, Stolper EM (1993) Noble gas solubilities in silicate melts and glasses: new experimental results for argon and the relationship between solubility and ionic porosity. Geochim Cosmochim Acta 57:5039–5051

Carroll MR, Webster JD (1994) Solubilities of sulfur, noble gases, nitrogen, chlorine, and fluorine in magmas. Rev Mineral 30:231–279

Danyushevsky L, Eggins S, Falloon T, Christie D (2000) H_2O abundance in depleted to moderately enriched mid-ocean ridge magmas; part I: incompatible behaviour, implications for mantle storage, and origin of regional variations. J Petrol 41:1329–1364

Dixon J, Stolper E, Holloway J (1995) An experimental study of water and carbon dioxide solubilities in mid-ocean ridge basaltic liquids. Part I: calibration and solubility models. J Petrol 36:1607–1631

Elkins-Tanton LT (2008) Linked magma ocean solidification and atmospheric growth for Earth and Mars. Earth Planet Sci Lett 271:181–191

Elkins-Tanton LT (2012) Magma oceans in the inner solar system. Ann Rev Earth Planet Sci 40:113–139

Elkins-Tanton L, Grove T (2011) Water (hydrogen) in the lunar mantle: results from petrology and magma ocean modeling. Earth Planet Sci Lett 307:173–179

Eugster HP, Wones DR (1962) Stability relations of the ferruginous biotite, annite. J Petrol 3:81–124

Foustoukos DI (2025) Molecular H_2 in silicate melts. Geochim Cosmochim Acta 389:125–135

Gaillard F, Schmidt B, Mackwell S, McCammon C (2003) Rate of hydrogen–iron redox exchange in silicate melts and glasses. Geochim Cosmochim Acta 67:2427–2441

Gaillard F, Bernadou F, Roskosz M, Bouhifd MA, Marrocchi Y, Iacono-Marziano G, Moreira M, Scaillet B, Rogerie G (2022) Redox controls during magma ocean degassing. Earth Planet Sci Lett 577:117244. https://doi.org/10.1016/j.epsl.2021.117255

Golabek G, Keppler H (2019) Graphite floatation on a magma ocean. and the fate of carbon during core formation. Geochem Persp Lett 11: 12-17

Hirschmann MM (2018) Comparative deep Earth volatile cycles: the case for C recycling from exosphere/mantle fractionation of major (H_2O, C, N) volatiles and from H_2O/Ce, CO_2/Ba, and CO_2/Nb exosphere ratios. Earth Planet Sci Lett 502:262–273

Hirschmann MM, Withers AC, Ardia P, Foley NT (2012) Solubility of molecular hydrogen in silicate melts and consequences for volatile evolution of terrestrial planets. Earth Planet Sci Lett 345–348:38–48

Ihinger PD, Hervig RL, McMillan PF (1994) Analytical methods for volatiles in glasses. Rev Mineral 30:67–121

Johnstone CP, Khodachenko ML, Lüftinger T, Kislyakova KG, Lammer H, Güdel M (2019) Extreme hydrodynamic losses of Earth-like atmospheres in the habitable zones of very active stars. Astronomy Astrophys 624:L10

Katyal N, Ortenzi G, Grenfell JL, Noack L, Sohl F, Godolt M, García Muñoz A, Schreier F, Wunderlich F, Rauer H (2020) Effect of mantle oxidation state and escape upon the evolution of Earth's magma ocean atmosphere. Astronomy Astrophysics 643: A81

Keppler H, Cialdella L, Couffignal F, Wiedenbeck M (2022) The solubility of N_2 in silicate melts and nitrogen partitioning between upper mantle minerals and basalt. Contrib Mineral Petrol 177:83

Luth RW, Mysen BO, Virgo D (1987) Raman spectroscopic study of the solubility behavior of H_2 in the system Na_2O-Al_2O_3-SiO_2-H_2. Am Mineral 72:481–486

Marty B (2012) The origins and concentrations of water, carbon, nitrogen and noble gases on Earth. Earth Planet Sci Lett 313–314:56–66

Michael P (1988) The concentration, behavior and storage of H_2O in the suboceanic upper mantle: implications for mantle metasomatism. Geochim Cosmochim Acta 52:555–566

Michael P (1995) Regionally distinctive sources of depleted MORB: evidence from trace elements and H_2O. Earth Planet Sci Lett 131:301–320

Moine BN, Bolfan-Casanova N, Radu IB, Ionov DA, Costin G, Korsakov AV, Golovin AV, Oleinikov OB, Deloule E, Cottin JY (2020) Molecular hydrogen in minerals as a clue to interpret δD variations in the mantle. Nat Comm 1:3604. https://doi.org/10.1038/s41467-020-17442-8

Ni H, Keppler H (2013) Carbon in silicate melts. Rev Mineral Geochem 75:251–287

Ohlhorst S, Behrens H, Holtz F (2001) Compositional dependence of molar absorptivities of near-infrared OH- and H_2O bands in rhyolitic to basaltic glasses. Chem Geol 174:5–20

Piani L, Marrocchi Y, Rigaudier T, Vacher LG, Thomassin D, Marty B (2020) Earth's water may have been inherited from material similar to enstatite chondrite meteorites. Science 369:1110–1113

Putak Juriček M, Keppler H (2024) Stability of hydrous basaltic melts at low water fugacity: evidence for widespread melting at the lithosphere-asthenosphere boundary. Contrib Mineral Petrol 179:97

Robie RA, Hemingway BS (1995) Thermodynamic properties of mineral and related substances at 298.15 K and 1 bar (10^5 Pascals) pressure and at higher temperatures. US Geol Surv Bull 2131:1–461

Rubie DC, Frost DJ, Mann U, Asahara Y, Nimmo F, Tsuno K, Kegler P, Holzheid A, Palme H (2011) Heterogeneous accretion, composition and core–mantle differentiation of the Earth. Earth Planet Sci Lett 301:31–42

Rubie DC, Jacobson SA, Morbidelli A, O'Brien DP, Young ED, de Vries J, Nimmo F, Palme H, Frost DJ (2015) Accretion and differentiation of the terrestrial planets with implications for the compositions of early-formed solar system bodies and accretion of water. Icarus 248:89–108

Saal A, Hauri E, Langmuir C, Perfit M (2002) Vapour undersaturation in primitive mid-ocean-ridge basalt and the volatile content of earth's upper mantle. Nature 419:451–455

Schmidt BC, Keppler H (2002) Experimental evidence for high noble gas solubilities in silicate melts under mantle pressures. Earth Planet Sci Lett 195: 277-290

Schmidt BC, Holtz F, Scaillet B, Pichavant M (1997) The influence of H_2O-H_2 fluids and redox conditions on melting temperatures in the haplogranite system. Contrib Mineral Petrol 126:386–400

Schmidt BC, Holtz FM, Bény JM (1998) Incorporation of H_2 in vitreous silica, qualitative and quantitative determination from Raman and infrared spectroscopy. J Non-Crystalline Solids 240:91–103

Schmidt BC, Holtz F, Pichavant M (1999) Water solubility in haplogranitic melts coexisting with H_2O-H_2-fluids. Contrib Mineral Petrol 136:213–224

Shelby JE (1994) Protonic species in vitreous silica. J Non-Cryst Solids 179:138–147

Shishkina T, Botcharnikov R, Holtz F, Almeev R, Portnyagin M (2010) Solubility of H_2O- and CO_2-bearing fluids in tholeiitic basalts at pressures up to 500 MPa. Chem Geol 277:115–125

Sossi PA, Tollan PME, Badro J, Bower DJ (2023) Solubility of water in peridotite liquids and the prevalence of steam atmospheres on rocky planets. Earth Planet Sci Lett 601:117894

Symonds RB, Rose WI, Bluth GJS, Gerlach TM (1994) Volcanic gas studies - methods, results, and applications. Rev Mineral 30:1–66

Truckenbrodt J, Johannes W (1999) H_2O loss during piston-cylinder experiments. Am Mineral 84:1333–1335

Vlasov K, Audétat A, Keppler H (2023) H_2–H_2O immiscibility in Earth's upper mantle Contrib Mineral Petrol 178:36

Walker JCG (1986) Impact erosion of planetary atmospheres. Icarus 68:87–98

Withers AC, Behrens H (1999) Temperature-induced changes in the NIR spectra of hydrous albitic and rhyolitic glasses between 300 and 100 K. Phys Chem Minerals 27: 119-132

Yang X, Keppler H, Li Y (2016) Molecular hydrogen in mantle minerals. Geochem Persp Lett 2:160–168
Young ED, Shahar A, Schlichting HE (2023) Earth shaped by primordial H_2 atmospheres. Nature 616:306–311

Publisher's note Springer Nature remains neutral with regard to jurisdictional claims in published maps and institutional affiliations.